

See discussions, stats, and author profiles for this publication at: <https://www.researchgate.net/publication/248024595>

# The thermal expansion and crystal structure of mirabilite ( $\text{Na}_2\text{SO}_4 \cdot 10\text{D}_2\text{O}$ ) from 4.2 to 300 K, determined by time-of-flight neutron powder diffraction

Article in *Physics and Chemistry of Minerals* · August 2009

DOI: 10.1007/s00269-008-0256-0

CITATIONS

43

READS

3,665

5 authors, including:



Helen Elizabeth Alexandra Brand

Australian Synchrotron

97 PUBLICATIONS 1,557 CITATIONS

SEE PROFILE

# The thermal expansion and crystal structure of mirabilite ( $\text{Na}_2\text{SO}_4 \cdot 10\text{D}_2\text{O}$ ) from 4.2 to 300 K, determined by time-of-flight neutron powder diffraction

H. E. A. Brand · A. D. Fortes · I. G. Wood ·  
K. S. Knight · L. Vočadlo

Received: 4 April 2008 / Accepted: 27 July 2008  
© Springer-Verlag 2008

**Abstract** We have collected high resolution neutron powder diffraction patterns from  $\text{Na}_2\text{SO}_4 \cdot 10\text{D}_2\text{O}$  over the temperature range 4.2–300 K following rapid quenching in liquid nitrogen, and over a series of slow warming and cooling cycles. The crystal is monoclinic, space-group  $\text{P}2_1/\text{c}$  ( $Z = 4$ ) with  $a = 11.44214(4)$  Å,  $b = 10.34276(4)$  Å,  $c = 12.75486(6)$  Å,  $\beta = 107.847(1)^\circ$ , and  $V = 1436.794(8)$  Å<sup>3</sup> at 4.2 K (slowly cooled), and  $a = 11.51472(6)$  Å,  $b = 10.36495(6)$  Å,  $c = 12.84651(7)$  Å,  $\beta = 107.7543(1)^\circ$ ,  $V = 1460.20(1)$  Å<sup>3</sup> at 300 K. Structures were refined to  $R_p$  (Rietveld powder residual,  $R_p = \sum |I_{\text{obs}} - I_{\text{calc}}| / \sum I_{\text{obs}}$ ) better than 2.5% at 4.2 K (quenched and slow cooled), 150 and 300 K. The sulfate disorder observed previously by Levy and Lisensky (Acta Cryst B34:3502–3510, 1978) was not present in our specimen, but we did observe changes with temperature in deuterium occupancies of the orientationally

disordered water molecules coordinated to Na. The temperature dependence of the unit-cell volume from 4.2 to 300 K is well represented by a simple polynomial of the form  $V = -4.143(1) \times 10^{-7} T^3 + 0.00047(2) T^2 - 0.027(2) T + 1437.0(1)$  Å<sup>3</sup> ( $R^2 = 99.98\%$ ). The coefficient of volume thermal expansion,  $\alpha_V$ , is positive above 40 K, and displays a similar magnitude and temperature dependence to  $\alpha_V$  in deuterated epsomite and meridianiite. The relationship between the magnitude and orientation of the principal axes of the thermal expansion tensor and the main structural elements are discussed; freezing in of deuterium disorder in the quenched specimen affects the thermal expansion, manifested most obviously as a change in the behaviour of the unit-cell parameter  $\beta$ .

**Keywords** Mirabilite · Sodium sulfate decahydrate · Thermal expansion · Neutron diffraction

**Electronic supplementary material** The online version of this article (doi:10.1007/s00269-008-0256-0) contains supplementary material, which is available to authorized users.

H. E. A. Brand (✉) · A. D. Fortes · I. G. Wood · L. Vočadlo  
Department of Earth Science, University College London,  
Gower Street, London WC1E 6BT, UK  
e-mail: helen.brand@ucl.ac.uk

H. E. A. Brand · A. D. Fortes · I. G. Wood · L. Vočadlo  
Centre for Planetary Sciences, University College London,  
Gower Street, London WC1E 6BT, UK

K. S. Knight  
ISIS Facility, Rutherford Appleton Laboratory, Chilton, Didcot,  
Oxfordshire OX11 0LA, UK

K. S. Knight  
The Natural History Museum, Cromwell Road,  
London SW7 5BD, UK

## Introduction

Sodium sulfate decahydrate— $\text{Na}_2\text{SO}_4 \cdot 10\text{H}_2\text{O}$ —is the stable phase in contact with an equilibrium mixture of  $\text{Na}_2\text{SO}_4$  and  $\text{H}_2\text{O}$  at room temperature and pressure (Fig. 1); the synthetic form of the substance is referred to as Glauber's salt, after its first manufacturer (Glauber 1658); and the naturally occurring form is the mineral mirabilite (e.g. Palache et al. 1951). The eutectic between mirabilite and ice Ih is at 271.85 K, 4.15 wt.%  $\text{Na}_2\text{SO}_4$ , and the solubility increases rapidly with temperature up to the peritectic at 305.534 K, 33.2 wt.%  $\text{Na}_2\text{SO}_4$  where mirabilite undergoes incongruent melting to anhydrous sodium sulfate (orthorhombic phase V, Fddd, thenardite). This is the highest dissociation temperature amongst the isostructural decahydrates of  $\text{Na}_2\text{SO}_4$ ,  $\text{Na}_2\text{SeO}_4$ ,  $\text{Na}_2\text{WO}_4$ ,

$\text{Na}_2\text{VO}_4$ , or  $\text{Na}_2\text{MoO}_4$ . Above this point, the solubility is retrograde, reaching a minimum near 400 K. A metastable phase,  $\text{Na}_2\text{SO}_4 \cdot 7\text{H}_2\text{O}$ , is known at room pressure and temperature (Löwel 1851, 1853, 1857; Viollette 1866; Tomlinson 1868, 1871; de Coppet 1907; Hartley et al. 1908; Wuite 1914; Hills and Wills 1938; Washburn and Clem 1938; Braitsch 1971; Gans 1978; Balarew 2002; Rijniers et al. 2005; Genkinger and Putnis 2007), although Löwel (1850) described an octahydrate, detailing the growth of large and beautiful prismatic crystals, and Genkinger and Putnis (2007) report a phase which does not match the X-ray diffraction patterns of either the decahydrate or heptahydrate; these or other hydration states may become stable at higher pressures (e.g. Hogenboom et al. 1999). The metastable heptahydrate–ice Ih eutectic is at 269.60 K, 12.8 wt.%  $\text{Na}_2\text{SO}_4$ , and the incongruent melting point of this phase is at 296.615 K (Washburn and Clem 1938).

Mirabilite forms abundant and widespread deposits on the Earth in association with salt domes and their related hydrocarbon reservoirs (Colman et al. 2002), with dislocations in thrust terrains, as a component of cold desert salt deposits (Keys and Williams 1981) and as the metasomatic products of the weathering of alkali igneous rocks (Hardie 1991). Commercially, mirabilite has long been recognised

for its possible use in the latent heat storage of thermal energy (Marliacy et al. 2000) and for its role in the weathering of building stone with high sodium sulfate content (Goudie and Viles 1997; Rijniers et al. 2005). Studies have shown that sodium sulfate causes more damage to building stone than any other salt. Damage occurs when dissolution of thenardite produces supersaturated solutions, which can lead to the precipitation of mirabilite in pore spaces. Commonly, the pressure generated by crystallisation of mirabilite exceeds the strength of the material (Tsui et al. 2003). Thermal expansion of the inter-pore precipitates also has a longer-term impact on the weathering of building stone.

The presence of soluble sulfates in chondritic meteorites has led to the suggestion that multiply hydrated salts such as mirabilite may also dominate the mantles of the icy moons of the Gas Giant planets (Kargel 1991). Evidence to support these models is provided by distorted  $\text{H}_2\text{O}$  absorption bands in the near infrared spectra of these satellites (observed by the Galileo space-craft between 1995 and 2003), interpreted as mixtures of Mg-,  $\text{Na}_2$ -, and/or  $\text{H}_2\text{SO}_4$ -hydrates (e.g., Dalton et al. 2005; Orlando et al. 2005), although there is some ambiguity concerning the identity and origin of the non-ice component (Carlson et al. 2007). In order to interpret the observed surface morphologies of the icy moons and to understand their thermal evolution, geophysical models of their interiors must be constructed. To do this we need to know the phase behaviour, thermoelastic, and transport properties of the constituent materials under the appropriate pressure and temperature conditions. Since these hydrated sulfate salts may experience hydrostatic pressures up to 1.5 GPa in the interiors of the largest icy moons, there has been interest recently in measuring the solubility and density of mirabilite at non-ambient conditions (e.g., Hogenboom et al. 1999; Dougherty 2006) to extend earlier high-pressure investigations into the pressure dependence of the ice–mirabilite eutectic (Block 1913; Geller 1924; Tammann 1929; Tanaka et al. 1992; Kryukov and Manikin 1960). These various experiments covered the range from 0 to 0.8 GPa, and 263 to 343 K; only Hogenboom et al. (1999) observed any evidence of another solid phase, which they identified tentatively as the heptahydrate, although Geller (1924) reported a branch in the peritectic melting point above 0.5 GPa.

Given the extraterrestrial significance of highly hydrated substances containing sulfate, we have been pursuing a program of research into their phase behaviour and physical properties (Fortes et al. 2006a, b, c, 2008a, b) with the ultimate objective of being able to understand better the internal structure and dynamics of large icy moons and to relate these findings to spacecraft observations of their surface geology (e.g., Fortes et al. 2007a).

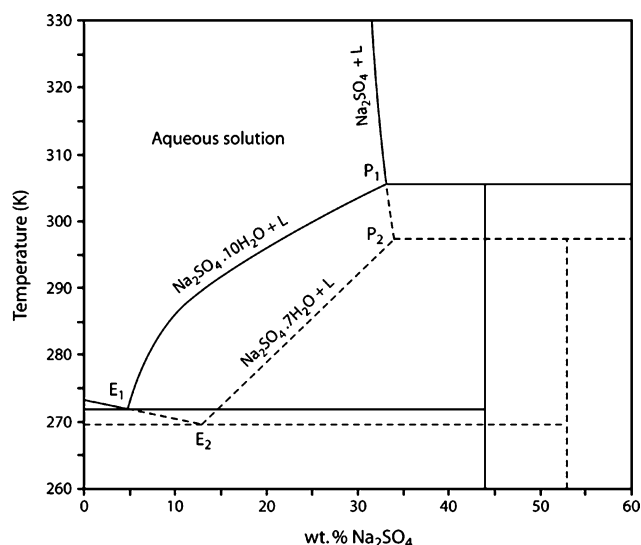


**Fig. 1**  $T$ - $X$  phase diagram of the binary system sodium sulfate–water at room pressure showing stable phase boundaries (solid) and metastable phase boundaries (dashed).  $E_1$  and  $E_2$  are the mirabilite–ice and the  $\text{Na}_2\text{SO}_4 \cdot 7\text{H}_2\text{O}$ –ice eutectics, respectively.  $P_1$  and  $P_2$  are the peritectics  $\text{Na}_2\text{SO}_4 \cdot 10\text{H}_2\text{O}(\text{s}) \leftrightarrow \text{Na}_2\text{SO}_4(\text{s}) + \text{liquid (L)}$  and  $\text{Na}_2\text{SO}_4 \cdot 7\text{H}_2\text{O}(\text{s}) \leftrightarrow \text{Na}_2\text{SO}_4(\text{s}) + \text{L}$ , respectively. The solid vertical line at 44.09 wt.%  $\text{Na}_2\text{SO}_4$  corresponds to the composition of mirabilite, and the dashed vertical line at 52.97 wt.% corresponds to the heptahydrate. Redrawn after Negi and Anand (1985) with solubility data tabulated in Garrett (2001, Table 7.1)

An integral part of this research involves the use of *ab initio* calculations (Fortes et al. 2006b) and interatomic potential calculations (Brand et al. 2006); both methods require high precision atomic coordinates at limiting low temperatures, whilst the latter requires precise structural data at a range of temperatures in order to achieve a good fit of the chosen potentials. Even in anhydrous  $\text{MgSO}_4$  there are subtle details of the thermal expansivity (Fortes et al. 2007b) which are a challenge for the interatomic potential method.

To date there have been few diffraction studies of mirabilite. The crystal system and unit cell shape were known from early goniometric analysis (e.g., Brooke 1824; Rosicky 1908; see von Groth 1908, pp. 371–372). The earliest X-ray data is presented by Hanawalt et al. (1938), in the form of relatively inexact *d*-spacings versus intensity. The unit cell dimensions and space-group were determined using single-crystal X-ray methods by Alietti (1959) and Cocco and Rossetti (1959), and the heavy atom structure was later solved, apparently independently, by Ruben et al. (1961) and Cocco (1962). Both studies obtained the same structure, although the latter displaces the unit cell origin by 0, 0, 1/2. Levy and Lisensky (1978) carried out a single-crystal neutron diffraction study, publishing accurate hydrogen atom positions.

The objectives of this work are to obtain structure refinements of mirabilite at liquid helium temperatures, and at a high homologous temperature and to measure precise lattice parameters over the intervening temperature range. Levy and Lisensky (1978), identified a complex pattern of disorder involving both the sulfate tetrahedra and the water molecule orientations; we were interested in studying the temperature dependence of this disorder since heat capacity measurements (Pitzer and Coulter 1938; Brodale and Giauque 1958; Ruben et al. 1961) indicate that the disorder becomes frozen in at limiting low temperatures. Our diffraction measurements also allow us to obtain the thermal expansion tensor as a function of temperature and to relate this to structural changes.

We begin by describing our sample preparation and data collection methods (“Experimental method”), and then present our results for, firstly, the crystal structure (“Results”), and, secondly, the thermal expansion of  $\text{Na}_2\text{SO}_4 \cdot 10\text{D}_2\text{O}$  (“Analysis of the thermal expansion”).

## Experimental method

### Sample preparation

The most suitable method for achieving our objectives is high resolution powder neutron diffraction. Given the large incoherent scattering cross section of the hydrogen atom,

we use a perdeuterated analogue in order to achieve good signal to noise in the measured diffraction data (e.g., Finney 1995). Deuteration is likely to have a minimal impact on the properties under investigation; by comparison with water ice, we would expect the unit cell of the deuterated isotopomer to be slightly larger (order 0.1%), and the bulk modulus to be slightly smaller (order 1%) than the hydrogen-bearing analogue. The work of Röttger et al. (1994) does not show a significant difference in volume thermal expansion between  $\text{D}_2\text{O}$  and  $\text{H}_2\text{O}$ .

The diffraction patterns were collected using the High Resolution Powder Diffractometer (HRPD) (Ibberson et al. 1992) at the STFC ISIS facility, Rutherford Appleton Laboratory, UK, which is ideally suited to rapid and accurate determination of cell parameters by virtue of its long neutron flight path (95 m) and essentially constant resolution ( $\Delta d/d = 4 \times 10^{-4}$  in the backscattering detectors,  $2\theta = 168.33^\circ$ ) across all *d*-spacings. Moreover, the instrument is sensitive to shifts in peak positions roughly two orders of magnitude smaller than the nominally stated resolution, by far the best resolution available in the world at present.

Crystals of perdeuterated mirabilite were grown from a supersaturated solution of  $\text{Na}_2\text{SO}_4$  (Sigma Ultra) in  $\text{D}_2\text{O}$  (Aldrich, 99 wt.% D) in a sealed flask. Large ( $\sim 1 \text{ cm}^3$ ) crystalline lumps of mirabilite were extracted from the mother liquor and characterised by powder X-ray diffraction prior to the experiment to confirm their phase identity. To prepare the sample for the neutron study, solid lumps of mirabilite were extracted from the liquor, dried on filter paper, and then quickly powdered in the ISIS cold room (to prevent dehydration) using an agate pestle and mortar; the resulting coarse powder was loaded into an aluminium-framed slab can with vanadium windows. During the data analysis (see below) we discovered that a small amount (order 1 wt.%) of  $\text{D}_2\text{O}$  ice Ih was present in the sample, which we suspect originated from aqueous solution adhering to the polycrystalline chunks after extraction from the mother liquor. Any ice formed from atmospheric water vapour would contain a large amount of  $^1\text{H}$ , resulting in an incoherent contribution to the background that is not apparent.

Gadolinium foil shielding was screwed over the front face of the can whilst a small electric heater and a RhFe temperature sensor were inserted into holes drilled in the aluminium frame to enable accurate measurement and control of the sample temperature. The sample can was screwed onto a cryostat centre stick and quenched to liquid nitrogen temperatures before being placed in a pre-cooled OC50 ‘Orange’ cryostat (AS Scientific, Abingdon, UK) mounted on the HRPD beamline.

The sample temperature was reduced to 4.2 K and data were collected in the backscattering detector banks, the  $90^\circ$

banks, and the low angle banks ( $2\theta = 30^\circ$ ) over the time-of-flight range 30–130 ms for 100  $\mu\text{A h}$ . Data were then collected upon warming of the sample from 10 to 300 K in 10 K increments, counting for approximately 20 min (7  $\mu\text{A h}$ ), at each datum, and allowing 10 min equilibration time. At 300 K, another long count (100  $\mu\text{A h}$ ) was undertaken to obtain another structural data set. Preliminary LeBail profile refinement of the warming data showed an abrupt change in the behaviour of the unit cell parameter  $\beta$  near 150 K; it was therefore decided to collect further data whilst the sample was cooled to 4.2 K (in 10 K steps interleaved between the warming points), again counting for 20 min (7  $\mu\text{A h}$ ), with 10 min of equilibration at each point. Further structural datasets (100  $\mu\text{A h}$ ) were collected at 4.2 K after the slow cooling, and at 150 K during a subsequent (second) slow warming run.

Data were normalised to the incident monitor spectrum and corrected for detector efficiency using a vanadium standard. After normalisation, the data were truncated to yield diffraction patterns over the  $d$ -spacing ranges 0.726–2.480 Å (backscattering), 1.017–3.180 Å ( $90^\circ$  banks), and 2.724–9.300 Å (low-angle banks), although additional ‘clipping’ at the shortest and longest flight time edges of the t-o-f windows was done during refinement to eliminate some residual normalisation errors.

### Data analysis

The data analysis was carried out using the Rietveld method implemented in the *General Structure Analysis System* (GSAS) package (Larsen and von Dreele 2000) with the EXPGUI user interface (Toby 2001). Commencing with the 4.2 K quenched dataset, the unit cell ( $a$ ,  $b$ ,  $c$ ,  $\beta$ ) and structural parameters ( $x$ ,  $y$ ,  $z$ ,  $U_{\text{iso}}$ ) of mirabilite, the unit cell of ice Ih ( $a$ ,  $c$ ), scale factors and phase fractions, background coefficients (12 term shifted Chebyshev polynomial), and profile coefficients ( $\sigma_1$  and  $\sigma_2$ ,  $\gamma_1$ ,  $L_{11}$ ,  $L_{22}$ ,  $L_{33}$  and  $\gamma_{1\text{ec}}$ ) were refined; the initial atomic coordinates are taken from Levy and Lisensky (1978) for mirabilite and from Fortes et al. (2004) for ice Ih. Soft bond length restraints were imposed upon the sulfate tetrahedra and the water molecules, fixing S–O = 1.47(2) Å and O–O = 2.39(2) Å (the latter forcing  $\angle\text{O–S–O} = 109 \pm 4^\circ$ ), O–D = 0.99(2) Å and D–D = 1.56(2) Å (forcing  $\angle\text{D–O–D} = 105 \pm 6^\circ$ ); the multiplier for the contribution from these restraints to the minimization function (FACTR) was set to 200. Isotropic temperature factors ( $U_{\text{iso}}$ ) for “like atoms” were constrained to be identical, these being grouped as: 1; Na atoms (Na2 and Na3), 2; S atoms, 3; sulfate oxygen atoms (O4–O7), 4; water oxygen atoms coordinated to Na (O8, O9, O12–O17), 5; other water oxygen atoms (O10 and O11), 6; deuterons H-bonded to sulfate oxygens (D8A, D9A, D10A, D10B, D11A, D11B,

D12B, D13B, D14B, D15B, D16A and D17A), 7; deuterons H-bonded to free water molecules (D12A, D13A, D14A, D15A) and 8; deuterons in the disordered ring (D8B, D8C, D9B, D9C, D16B, D16C, D17B and D17C). Sample texture was modelled using the spherical harmonic model implemented in GSAS (to 10th order for mirabilite only). Although the sample was not strongly textured, it was found to have a significant effect on the refined values of the structural parameters, and gave improved agreement factors. Finally, we found that it was necessary to include an extinction correction to avoid negative temperature factors; this is likely due to the coarse nature of the powder produced as we wished to avoid dehydrating the sample by excessive grinding.

It was found that the use of a single set of texture parameters for all three detector banks introduced bias into the refinements since the  $90^\circ$  and low-angle detectors, unlike the backscattering detectors, do not collect data from the whole Debye–Scherrer ring; for any structural model, the agreement of fit for each bank could be improved if the texture index for that bank was allowed to refine.

It was decided, therefore, that the backscattering data alone should be used for refinement of the structural model since the vast majority of the Bragg reflections (3911) were observed in the highest resolution backscattering data, whereas the  $90^\circ$  data contained only an additional 37 reflections (1291 reflections in total in the backscatter banks from mirabilite) and the low angle bank an additional 50 mirabilite reflections (only 96 reflections in total in this bank). As a final check of the validity of this procedure, the structural model obtained by fitting to the backscattering data was then fixed and used to fit the  $90^\circ$  and low-angle data varying only the background and peak profile coefficients, scale factors, the diffractometer constants DIFA and DIFC (related to the neutron time-of-flight as,  $\text{t-o-f} = \text{DIFA} \cdot d^2 + \text{DIFC} \cdot d + \text{ZERO}$ ,  $d$  being the  $d$ -spacing, and ZERO being another diffractometer constant which we did not refine), and the spherical harmonic texture coefficients.

In the later stages of the refinement, the fractional occupancies of the disordered atoms described by Levy and Lisensky (1978)—see “Crystal structure of mirabilite at 4.2, 150 and 300 K” below—were allowed to vary. As with the hexagonal ring of water molecules seen in the ice Ih structure, the square ring of Na-coordinated water molecules within the mirabilite structure is formed of disordered hydrogen bonds, each O...O vector having two half-occupied hydrogen sites at high temperatures. The occupancies of these sites (constrained to sum to 1) were refined and we obtained consistent and physically meaningful results. Levy and Lisensky (1978) also identified two orientations for the sulfate tetrahedra in the structure, and occupancies



of  $\sim 75:25$  at room temperature, with correspondingly occupied sites for the hydrogen atoms bonded to the sulfate oxygens. However, our refinement of the sulfate site occupancies resulted in a shift from 75:25 to 100:0. This occurred in all four structural datasets; we took great care in testing the effect on  $\chi^2$  of fixing partial occupancies on these sites, and we must conclude that our data can only be consistent with ordered sulfate tetrahedra and ordered hydrogen bonds donated to the tetrahedra's apices.

The quality of all of the fits to the data collected for long counting times, as exemplified by the 4.2 K slow cooled fit in Fig. 2 and reported as Rietveld powder statistics in the electronic supplementary tables, is very good, even in the 90° and low-angle banks where the structural model was fixed;  $R_p$  values are all below 2.5% for the 4.2 K slow cooled data. The texture index of mirabilite is  $\approx 1.01$ , indicative of a well randomised powder, and the refined phase fraction of mirabilite is 0.986(3). Note that the extinction coefficient (reported in the electronic supplement) is much higher at 300 K than it is at lower temperatures; this is probably due to grain growth since the specimen was above its binary eutectic temperature (Fig. 1) and a small amount of partial melting (estimated from the phase diagram to be 3–4 wt.%) must have occurred; this is also reflected in an increase and change in form of the background in the diffraction pattern at 300 K.

## Results

### Crystal structure of mirabilite at 4.2, 150 and 300 K

The unit cell dimensions obtained from the four structural refinements are shown in Table 1; atomic coordinates, and selected interatomic bond distances and angles at each temperature are given in electronic supplementary tables. Whilst these results do not offer a significant improvement in uncertainty on the atomic coordinates over Levy and Lisenky's (1978) single-crystal study, we have been able to determine the temperature dependence of key structural parameters which may be related to the anisotropy of the thermal expansion, as described in the subsequent section. The agreement between our 300 K deuterated unit cell and the 298 K hydrogenous unit cell (Levy and Lisenky 1978) is excellent; only  $\beta$  differs by more than  $2\sigma$ .

As shown in Fig. 3a, the structure of mirabilite consists of edge sharing  $\text{Na}(\text{H}_2\text{O})_6$  octahedra arranged in sinuous ribbons extending along the  $c$ -axis, with a net stoichiometry of  $\text{Na}_2(\text{H}_2\text{O})_8$ . The octahedra comprise  $\text{H}_2\text{O}$  molecules, labelled in the supplementary tables as O8, O9, and O12–O17, with O12–O15 forming the shared edges.

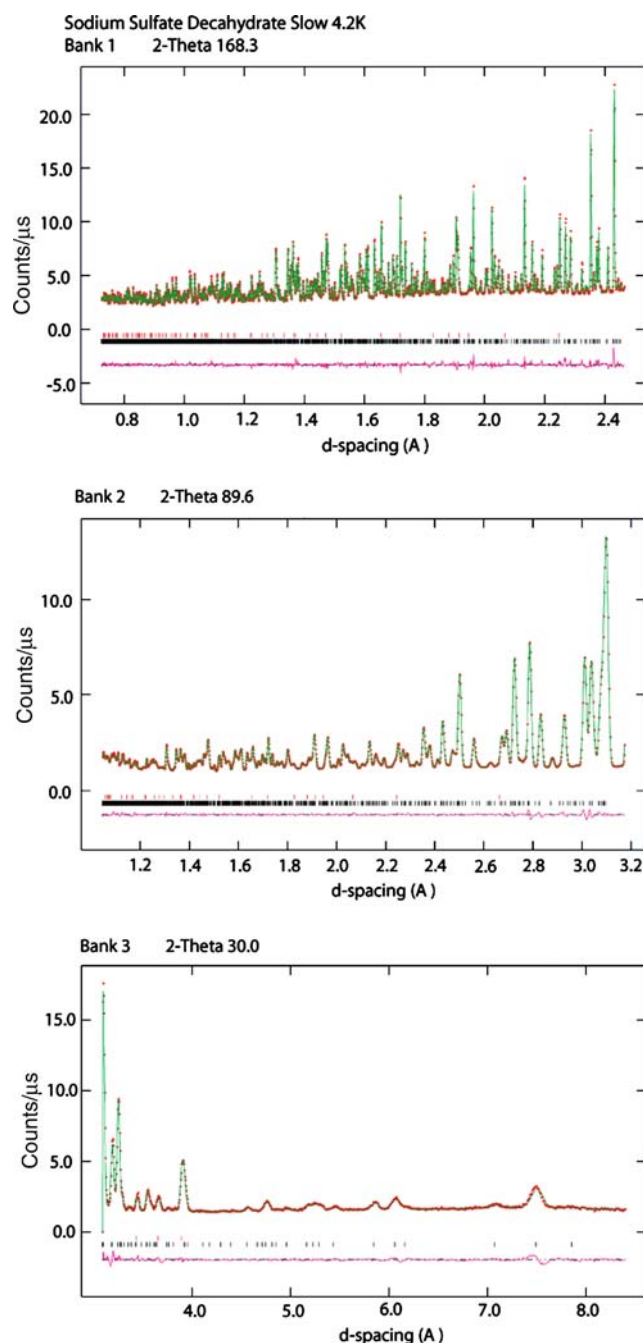


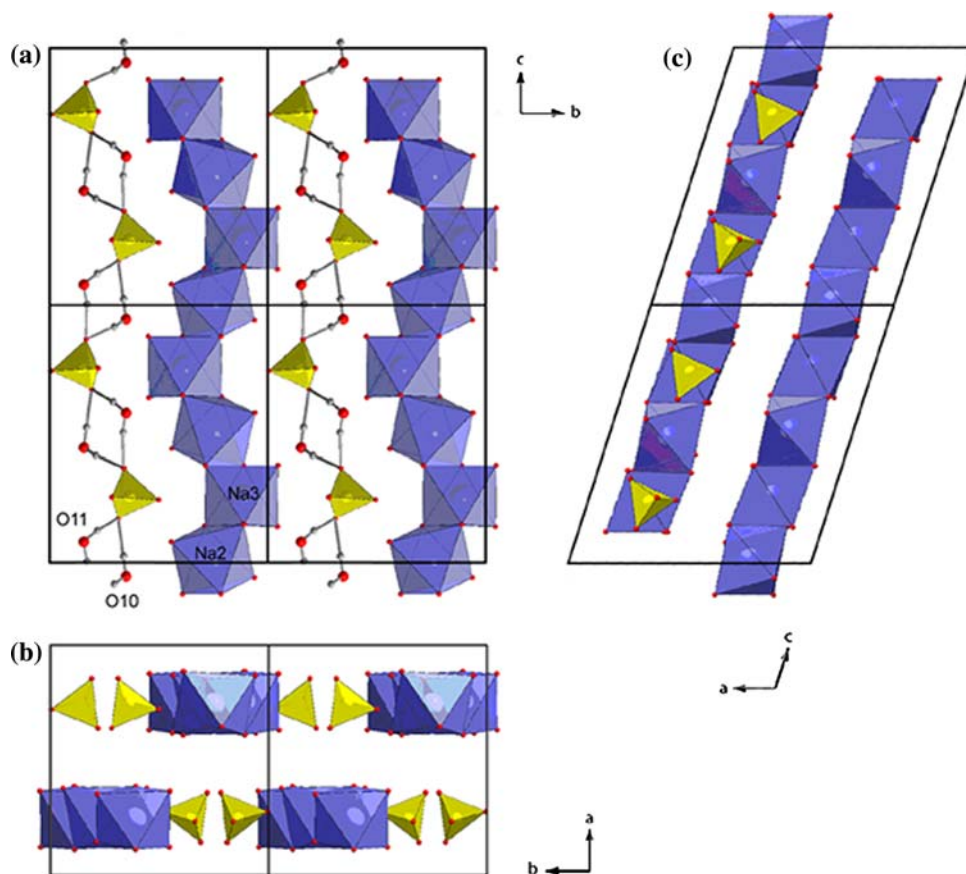
**Fig. 2** Neutron powder diffraction patterns of mirabilite at 4.2 K obtained on HRPD (i) from the backscattering banks, (ii) from the 90° banks and (iii) from the 30° banks. In each case the red circles are the observations, the green line the fit to the observations and the pink line below is the difference between the fit and the observations. The lower set of black tick marks denote the positions of the mirabilite peaks and the upper set of red tick marks are the positions of  $\text{D}_2\text{O}$  ice Ih peaks

These ribbons of octahedra alternate with chains of sulfate tetrahedra (oxygen O4–O7) and the two are linked together by the remaining water molecules (labelled O10 and O11), that are not coordinated to Na. The alternating ribbons of  $\text{Na}_2(\text{H}_2\text{O})_8$  and  $\text{SO}_4$  tetrahedra +  $\text{H}_2\text{O}$  thus form

**Table 1** Comparison of the unit cell dimensions of mirabilite at 4.2 K (slow cooled and quenched), 150 and 300 K with the published values of Levy and Lisensky (1978)

	4.2 K quenched	4.2 K slow cooled	150 K	300 K	298 K L & L (1978)
$a$ (Å)	11.44190(6)	11.44214(4)	11.46417(5)	11.51473(7)	11.512(3)
$b$ (Å)	10.34307(5)	10.34276(4)	10.34689(5)	10.36496(6)	10.370(3)
$c$ (Å)	12.75316(6)	12.75468(6)	12.77201(6)	12.84653(7)	12.847(2)
$\beta$ (°)	107.838(1)	107.847(1)	107.826(1)	107.7545(1)	107.789(10)
Volume (Å <sup>3</sup> )	1436.714(8)	1436.794(8)	1442.266(8)	1460.20(1)	1460.3(5)

**Fig. 3** Polyhedral representation of the mirabilite structure, with the unit cell outlined in black: **a** view along the  $a$ -axis, **b** along the  $c$ -axis, and **c** along the  $b$ -axis. The  $\text{Na}(\text{H}_2\text{O})_6$  octahedra are shown in dark blue and the  $\text{SO}_4$  tetrahedra in yellow. The interstitial  $\text{H}_2\text{O}$  molecules are shown, but the H-atoms bonded to the  $\text{Na}(\text{H}_2\text{O})_6$  octahedra have been omitted for clarity



a flat sheet extending in the  $b$ – $c$  plane (Fig. 3b, c). The sheets are stacked A–B–A–B along the  $a$ -axis, being connected by a combination of orientationally ordered and disordered hydrogen bonds. This layering accounts for the perfect cleavage on {100} (Palache et al. 1951). Figure 4 is a connectivity map revealing the patterns of bonding between the various structural elements, in particular the extensive hydrogen bonding within the structure (cf. Ruben et al. 1961).

The heat capacity data (Pitzer and Coulter 1938; Brodale and Giauque 1958; Ruben et al. 1961) were used to infer that hydrogen bonds in the mirabilite structure were

disordered, and that this disorder became frozen-in at limiting low temperatures. In their single-crystal study, Levy and Lisensky (1978) identified two areas of orientational disorder, the first associated with a pair of square rings between adjacent octahedral apices, and the second associated with the sulfate tetrahedra. The square rings involve the molecule pairs O8/O16 (ring 1, shown in Fig. 5) and O9/O17 (ring 2) which form the apices of Na octahedra and donate hydrogen bonds to sulfate oxygens O5 and O7 (ring 1) and O4 and O6 (ring 2).

Each corner of the ring donates and receives one hydrogen bond from a neighbouring corner, with two

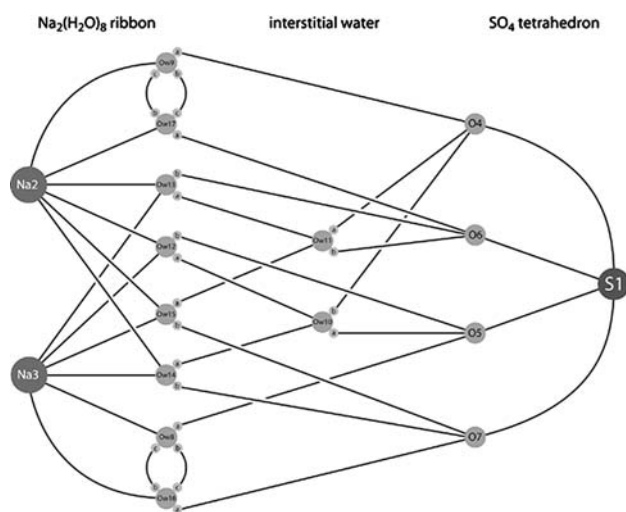


**Fig. 4** Connectivity map illustrating the relationship between structural elements in mirabilite. Note that the disorder involving the sulfate tetrahedron (and associated hydrogen bonds) has been left out; the hydrogen bond structure depicted corresponds to the fully ordered sulfate orientations obtained in this work

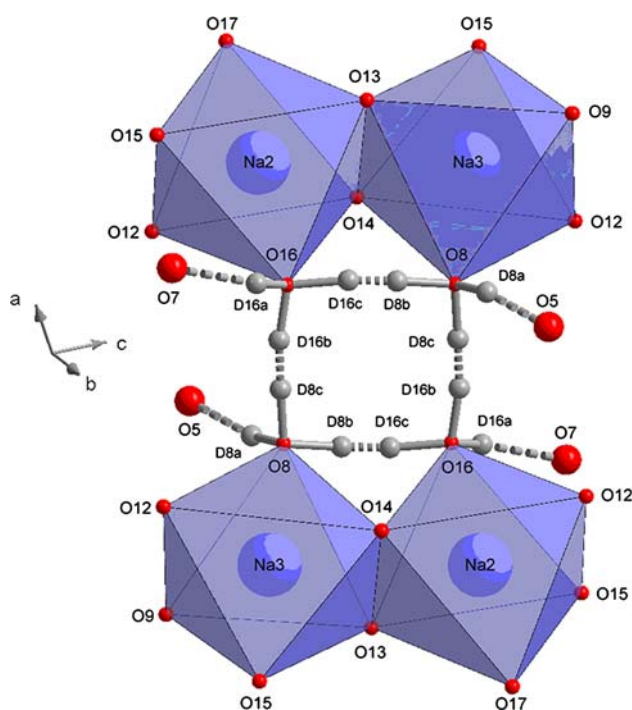


**Fig. 5** One of the square rings of water molecules involving disordered hydrogen bonds. The twofold axis of rotational symmetry passes through the middle of the ring, although not quite perpendicular to the plane of the page, as shown by the unit-cell axes

possible orientations denoted 'b' and 'c' (the 'a' hydrogens are donating bonds to the sulfate oxygens). In any one ring, all hydrogens must all be on either the 'b' sites or all on the 'c' sites, although a small fraction of rings will contain a mixture of 'b' and 'c' orientations along with Bjerrum

**Table 2** The refined fractional occupancies (constrained to sum to unity) of deuterons in the square rings defined by oxygen atoms O8/O16 (ring 1) and O9/O17 (ring 2) as a function of temperature

Species	300 K	150 K	Slow cooled 4.2 K	Quenched 4.2 K
'b'	0.494(6)	0.652(5)	0.693(4)	0.654(5)
'c'	0.506(6)	0.348(5)	0.307(4)	0.346(5)

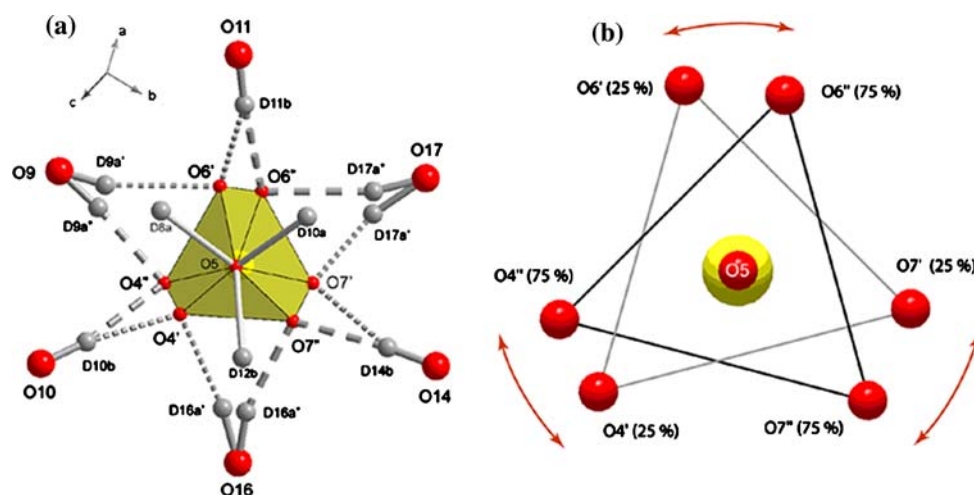
defects. Thermally activated hopping between sites means that the time- and space-averaged structure sensed by our diffraction experiment will observe two partially occupied sites (both 'b' and 'c') along each O...O vector of the ring. Complete orientational disorder corresponds to 50:50 occupancy of the 'b' and 'c' sites, whereas complete orientational order corresponds to either 100:0 or 0:100 occupancy of these sites. Levy and Lisensky (1978) refined this ratio = 50:50 at room temperature.

Our results at 300 K show complete orientational disorder; the occupancy ratios of the 'b' and 'c' sites in both rings are 49.4(6):50.6(6). As the temperature is reduced slowly, the trend is towards greater orientational order, the 'b' site having the larger occupancy. On the timescale of our experiments, full orientational order was not achieved at liquid helium temperatures, the 'b':'c' occupancy ratio being ~70:30 (see Table 2), although it is possible that sufficiently long timescales at low temperatures (e.g., on the surfaces of icy moons in the outer solar system) will permit full ordering of these sites to be attained. This is in agreement with measurements of the heat capacity as a function of temperature (Pitzer and Coulter 1938; Brodale and Giauque 1958; Ruben et al. 1961). More rapid cooling (in this instance, quenching in liquid nitrogen) results in a disequilibrium value for the occupancies becoming frozen-in. The refined occupancies from the quenched sample measured at 4.2 K are the same as those observed in the slow-cooled sample measured at 150 K (65:35) (see Table 2). As discussed in "Analysis of the thermal expansion", the variation of the unit-cell parameter  $\beta$  appears to support the hypothesis that this orientational disorder becomes frozen in near 150 K when mirabilite is quenched rapidly.

Levy and Lisensky also identified disorder over two orientations of the sulfate tetrahedra, which they denoted with 'prime' and 'double-prime' superscripts. The two orientations, related by a rotation of about 30° about the S...O5 vector (Fig. 6), generate pairs of partially occupied sulfate oxygen sites (O4'/O4'', O6'/O6'', and O7'/O7'' in their notation), which Levy and Lisensky (1978) found to be occupied in the ratio  $\approx 25:75$  (Fig. 6b). The sulfate apices accept hydrogen bonds from neighbouring water molecules. The bonds donated to the O5 apex (from D8a,



**Fig. 6** The two orientations of the sulfate tetrahedron described by Levy and Lisensky (1978) as viewed down the rotation axis (the S...O5 vector)—orientation relative to the crystallographic axes is shown by the legend in **a**. The hydrogen bonds donated to the ordered apex (O5) are shown with solid grey rods; those donated to the lesser occupied apices (O4', O6', and O7') are depicted as thinner, short-dashed rods; those donated to the more fully occupied apices (O4'', O6'', and O7'') are depicted as thicker, long-dashed rods



D10a, and D12b) are fully ordered. The bonds to the partially occupied apical sites are a mixture of ordered hydrogen bonds (donated by D10b, D11b, and D14b) and disordered hydrogen bonds (donated by D9a'/D9a'', D16a'/D16a'', and D17a'/D17a''). In Levy and Lisensky's refinement of the structure the occupancies of these hydrogen sites share the same occupancy as the apical oxygen sites; i.e., the 'primed' sites are  $\sim 25\%$  occupied, and the 'double-primed' sites are  $\sim 75\%$  occupied. Notice that the proposed switch in orientation from 'prime' to 'double-prime' involves breaking of the hydrogen bonds donated by D9a', D16a', and D17a' (the thicker, long-dashed bonds in Fig. 6a), and the formation of new hydrogen bonds from D9a'', D16a'', and D17a'' (the thin, short-dashed bonds in

Fig. 6a). Levy and Lisensky (1978) used the room temperature occupancies to determine the energy difference between the two orientations as  $2713 \pm 197 \text{ J mol}^{-1}$ , which is approximately 10% of the energy contained in a single hydrogen bond.

Our refinement of these site occupancies yielded ratios of 'prime':'double-prime' = 0:100 at all temperatures and this was confirmed by production of a Fourier difference map in GSAS. This is the sole point of significant disagreement between our work and that of Levy and Lisensky; it is plausible that the difference is the result of deuteration, or that it is due to the thermal history of the sample during the diffraction data collection, or some other aspect of the crystal growth or sample preparation.

**Table 3** Changes in the size and shape of the  $\text{Na}(\text{H}_2\text{O})_6$  octahedra with temperature. Volumes and distortion parameters (as defined by Robinson et al. 1971) were calculated using the program DRAWxtl (Finger et al. 2007)

	300 K	150 K	Slow cooled 4.2 K	Quenched 4.2 K
Na2 octahedron				
Volume ( $\text{\AA}^3$ )	19.719	19.854	19.813	19.854
Distance variance	$1.7 \times 10^{-4}$	$5 \times 10^{-5}$	$8 \times 10^{-5}$	$1.3 \times 10^{-4}$
Quadratic elongation	0.98215	0.96076	0.95865	0.95943
Angle variance	1613.163	1542.025	1538.271	1538.441
Na3 octahedron				
Volume ( $\text{\AA}^3$ )	20.317	19.977	19.913	19.918
Distance variance	$9 \times 10^{-4}$	$3.1 \times 10^{-4}$	$2.5 \times 10^{-4}$	$2 \times 10^{-4}$
Quadratic elongation	0.94877	0.95016	0.94941	0.94926
Angle variance	1512.895	1509.775	1508.869	1511.638
Thenardite <sup>a</sup>				
Volume ( $\text{\AA}^3$ )	25.500	—	—	—
Distance variance	$1.0 \times 10^{-3}$	—	—	—
Quadratic elongation	0.82596	—	—	—
Angle variance	1026.973	—	—	—

<sup>a</sup> Rasmussen et al. (1996)

The volumes and distortion parameters of the two symmetry-independent  $\text{Na}(\text{H}_2\text{O})_6$  octahedra as a function of temperature are given in Table 3. Because of the larger ionic radius and lower charge of the  $\text{Na}^+$  ion relative to the  $\text{Mg}^{2+}$  ion, these octahedra have a volume  $\sim 65\%$  greater than in the  $\text{Mg}(\text{H}_2\text{O})_6$  octahedra found in Mg-sulfate hydrates, but exhibit the same trend towards smaller volume and less distortion with increasing hydration number: room temperature data for anhydrous  $\text{Na}_2\text{SO}_4$ , thenardite, are compared in Table 3 where it can be seen that the volumes of the two mirabilite  $\text{Na}(\text{H}_2\text{O})_6$  octahedra are both much smaller than that of the  $\text{NaO}_6$  octahedron of thenardite. Upon cooling to 4.2 K, the Na2 octahedron in mirabilite increases in volume by 0.7% whereas the Na3 octahedron shrinks by 2%, the former being similar to the increase in volume (1–2%) observed in epsomite and meridianiite (Fortes et al. 2006b, 2008b).

The Na–O distances between apical oxygens, and shared-edge oxygens follow the same trend, the former shrinking from a mean of 2.420(8) Å at 300 K to a mean of 2.394(4) Å at 4.2 K ( $\Delta L/L = -1.1 \pm 0.1\%$ ); the latter shrink from a mean of 2.425(5) Å at 300 K to a mean of 2.408(3) Å at 4.2 K ( $\Delta L/L = -0.7 \pm 0.2\%$ ).

Since the S–O bond lengths and angles in the sulfate tetrahedron were restrained, it is not possible to draw any conclusions as to the temperature dependent behaviour of this unit; however, Fortes et al. (2008b) noted that there was a negligible change in the volume of sulfate tetrahedra with temperature in a range of anhydrous and hydrated Mg-sulfate crystals.

There are four types of hydrogen bond in the mirabilite structure, which may or may not behave differently with temperature; there are (1) those donated by Na-coordinated waters to other Na-coordinated waters (i.e., those involved in the square rings); (2) those donated by Na-coordinated waters to interstitial waters; (3) those donated by Na-coordinated waters to sulfate oxygens; and finally 4) those donated by interstitial waters to sulfate oxygens. It is interesting to note that the deuteron disorder is confined to the type 1 bond.

At 4.2 K H-bond types 1–4 have mean lengths of 1.797(2), 1.840(3), 1.859(3), and 1.848(2) Å, respectively. At 300 K, the mean lengths of these bonds are, respectively, 1.7995(4), 1.8508(5), 1.8500(4), and 1.910(3) Å. The difference in the mean length of hydrogen bond type 1 is not significantly different from zero ( $0.003 \pm 0.002$  Å), and in the type 2 and 3 bonds it is very small ( $0.010 \pm 0.004$  Å). However, the type 4 H-bonds, those donated by interstitial waters to sulfate oxygens, exhibit a significant increase in their mean length on warming from 4.2 to 300 K ( $0.062 \pm 0.005$  Å). This behaviour is similar to that observed in  $\text{MgSO}_4 \cdot 11\text{D}_2\text{O}$  where the water–water

H-bonds do not change in length, but the water–sulfate H-bonds increase in length significantly upon warming (Fortes et al. 2008b).

The type 1 hydrogen bonds which form the disordered ring structure exhibit insignificant differences in length between quenched and slow cooled specimens. The average quenched and slow cooled values of bond lengths are 1.802(3) and 1.797(2) Å, respectively.

Considering the hydrogen bond angles ( $\angle \text{O} \cdots \text{D} \cdots \text{O}$ ), type 2 are the most linear ( $172 \pm 0.2^\circ$ ) and type 1 are the least linear ( $164 \pm 0.2^\circ$ ) at 4.2 K. This bond angle does not change significantly with temperature across types 1–3 ( $<1\%$ ). However, the average value for type 4 H-bonds changes by  $6(1)^\circ$  (4%) revealing that much of the strain in the structure is accommodated by bending of bonds donated by interstitial water molecules.

### Analysis of the thermal expansion

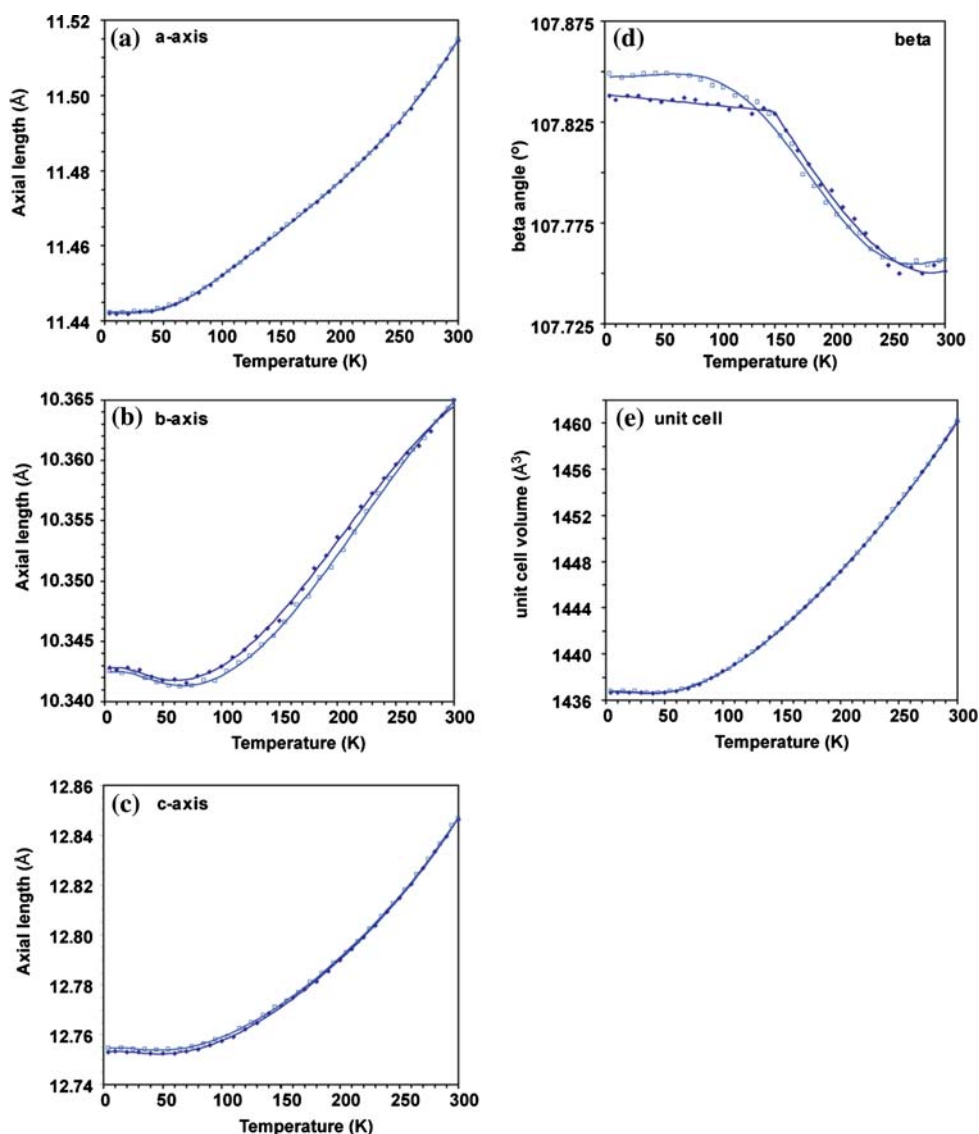
Lattice parameters ( $a$ ,  $b$ ,  $c$ ,  $\beta$ ) for mirabilite were obtained at 31 temperatures from 4.2 to 300 K (in 10 K increments) during slow warming of the initially quenched sample, and at 30 temperatures from 300 to 4.2 K (also in 10 K increments during slow cooling): these data are reported in Fig. 7. Rietveld refinement of these 7  $\mu\text{A h}$  datasets yielded unit cell parameters with a precision of  $\sim 3$  parts in 100,000, which is comparable to the precision we achieved in our study of  $\text{MgSO}_4 \cdot 7\text{D}_2\text{O}$  (Fortes et al. 2006b) and  $\text{MgSO}_4 \cdot 11\text{D}_2\text{O}$  (Fortes et al. 2008b).

### Volume thermal expansion

Using the results obtained from the refinements of the powder diffraction data we were able to calculate the volume and axial thermal expansivities of mirabilite over the temperature range 4.2–300 K. The volume thermal expansion is positive and normally behaved above 40 K, below which it is slightly negative, as can be seen in Fig. 8 where the volume thermal expansion coefficient  $\alpha_V$ , for deuterated mirabilite from Debye (solid line) and Einstein (dotted line) models are shown. The dashed line shows the volume thermal expansion of meridianiite (Fortes et al. 2008b) for comparison.

For the purpose of making a simple density calculation (e.g., for planetary interior modelling), we have fitted a third order polynomial to the density of mirabilite calculated from the unit-cell volume between 50 and 300 K,  $\rho/\rho_0 = AT^3 + BT^2 + CT + 1$ . The coefficients obtained are,  $A = 2.9(1) \times 10^{-11} \text{ K}^{-3}$ ,  $B = -3.19(5) \text{ K}^{-2}$ ,  $C = 1.61(5) \text{ K}^{-1}$  with  $\rho_0 = 1527.85 \text{ kg m}^{-3}$  for deuterated mirabilite ( $R^2 = 99.986\%$  and the maximum density difference between the observed data and those

**Fig. 7** The temperature dependent variation of the unit cell parameters; **a** *a*-axis; **b** *b*-axis; **c** *c*-axis; **d** monoclinic angle  $\beta$ ; **e** unit cell volume, over the temperature range 4.2–300 K. Values obtained upon warming of the quenched specimen are shown as *filled diamonds*, and those obtained during subsequent slow cooling of the specimen equilibrated at 300 K are shown as *open squares*. Standard errors are comparable in size to the symbols used. The solid lines shown in **a–c** and **e** are Einstein model fits to both data sets (Eqs. 9, 10); and the lines shown in **d** are polynomial fits; for details see text



from the polynomial fit is 0.012%). Assuming that the unit cell volume of *protonated* mirabilite shows the same temperature dependence as the deuterated isotopomer, then for  $\text{Na}_2\text{SO}_4 \cdot 10\text{H}_2\text{O}$   $\rho_0 = 1489.63 \text{ kg m}^{-3}$ .

A more physically meaningful interpretation of the thermal expansion curve can be obtained by using Grüneisen approximations for the zero-pressure equation of state (see Wallace 1998), in which the effects of thermal expansion are considered to be equivalent to elastic strain induced by the thermal pressure. These take the form, to first order,

$$V(T) = V_0 + \frac{\gamma U}{K_0} \quad (1)$$

and to second order,

$$V(T) = V_0 \left[ 1 + \frac{U}{Q - bU} \right] \quad (2)$$

where  $Q = (V_0 K_0 / \gamma)$  and  $b = 1/2 (K'_0 - 1)$ ;  $V_0$  is the unit cell volume at zero pressure and temperature,  $K_0$  is the zero pressure and temperature bulk modulus,  $K'_0$  is its first derivative with respect to pressure, and  $\gamma$  a Grüneisen parameter (assumed constant). The internal energy of the crystal,  $U(T)$ , may be calculated via the Debye approximation for the heat capacity,

$$U(T) = 9Nk_B T \left( \frac{T}{\theta_D} \right)^3 \int_0^{\theta_D/T} \frac{x^3}{e^x - 1} dx \quad (3)$$

where  $\theta_D$  is the Debye temperature,  $N$  is the number of atoms per unit cell,  $k_B$  is the Boltzmann constant, and  $x = \hbar\omega/k_B T$ . Note that the vibrational zero-point energy of  $9Nk_B\theta_D/8$  is included in Eq. 2 via the term  $V_0$ . The integral is evaluated numerically.

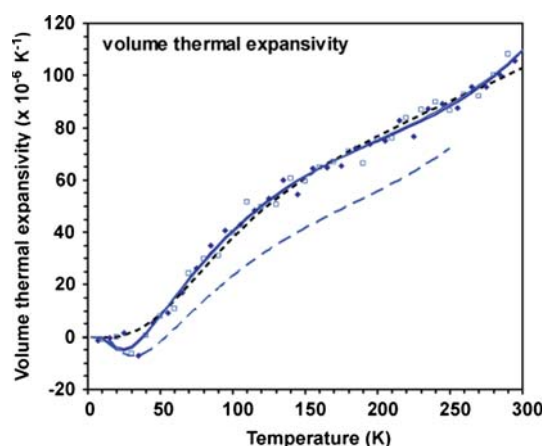


**Fig. 8** Comparison of the volume thermal expansion coefficient  $\alpha_V$ , for deuterated mirabilite: **a** as calculated via Eq. 2 and the heat capacity data (dotted line); **b** via the Einstein model (solid lines), fitted to both data sets, for details see text. The points shown were obtained from simple point by point numerical differentiation of the refined unit-cell volumes; values upon warming of the quenched specimen are shown as filled diamonds and those obtained on subsequent slow cooling as open squares. Note the misfit below 40 K. The dashed line shows the volume thermal expansion of meridianiite (Fortes et al. 2008b) for comparison

Least-squares fitting of the first-order approximation (Eq. 1) to our  $V(T)$  data yielded the parameters  $\theta_D = 529(8)$  K,  $V_0 = 1436.72(4) \text{ \AA}^3$ ,  $Q = 5.56(7) \times 10^{-17}$  J. This value of  $Q$  gives a value of  $K_0/\gamma = 39(1)$  GPa.

When the second-order approximation was fitted, the values of the variable parameters were found to  $\theta_D = 441(3)$  K,  $V_0 = 1436.66(3) \text{ \AA}^3$ ,  $Q = 7.3(3) \times 10^{-17}$  J and  $b = 11(2)$ ; these imply  $K_0/\gamma = 51(2)$  GPa and  $K'_0 = 23(4)$ . In both of these approximations the values of  $K_0$  and  $K'_0$  in the second case, are much higher than might reasonably be expected and so, in order to try to obtain more realistic elastic parameters, Eq. 2 was employed but with the internal energy term calculated via the available heat capacity data (Brodale and Giauque 1958; note, however, that these values are for hydrogenous, rather than deuterated mirabilite). In order to do this it is necessary to have an expression which can be integrated for  $C_V(T)$ . A fit of the heat capacity data to a single Debye model proved poor so a three-region empirical polynomial approach was employed, the coefficients of which are reported in

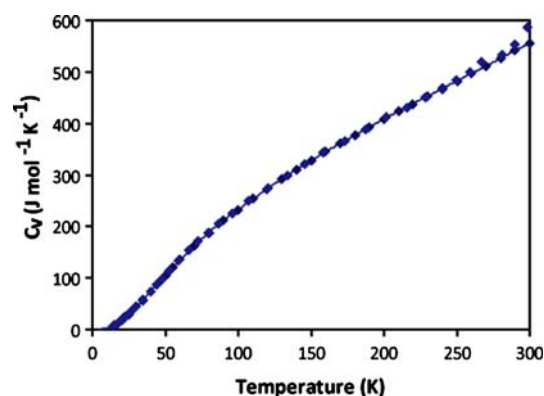


**Fig. 9** Fit of experimental heat capacity data (open circles) taken from Brodale and Giauque (1958) and converted to  $C_V$  values (see text). Three polynomials were used for different temperature ranges, as shown in Table 4. The corresponding values from Pitzer and Coulter (1938) are also shown in the figure (closed circles), but these were not included in the fitting

Table 4, and  $U(T)$  was then determined by integration of these polynomials; before fitting, the published  $C_p$  values were converted to  $C_V$  values using the expression  $C_p = C_V(1 + \alpha_V \gamma T)$ ; the values of  $\alpha_V T$  were taken from our measurements and  $\gamma$  was assumed to be 1.3. Figure 9 shows the fit of these polynomials to the modified heat capacity data.

With  $U(T)$  calculated from the specific heat data, the second-order approximation gave good agreement with the data above 40 K; below this temperature it is unable to accommodate the negative thermal expansion of the crystal (see Fig. 8). The values of the fitted parameters were:  $V_0 = 1436.41(7) \text{ \AA}^3$ ,  $Q = 4.2(1) \times 10^{-17}$  J and  $b = 9(2)$ , values for  $K_0/\gamma = 29(1)$  GPa, and  $K'_0 = 19(4)$ . Once again, these results are much higher than might be expected but are comparable to those previously obtained by Fortes et al. (2006b) using a similar procedure, for epsomite where it was found that  $K_0/\gamma = 31.9(3)$  GPa and  $K'_0 = 26(1)$ . The failure of this approximation to produce realistic values of  $K_0$  and  $K'_0$  is interesting as for non-molecular solids such as FeSi, (Vočadlo et al. 2002),  $\text{KMgF}_3$  (Wood et al. 2002), this technique has been used successfully, producing reasonable elastic parameters. It is possible that epsomite and mirabilite show a greater temperature dependence of  $\gamma$  and  $K_0$ , which are both assumed to be constant in this

**Table 4** Coefficients of the polynomial fits to the heat capacity data (see Fig. 9); these take the form  $C_V(T) = A + BT + CT^2 + DT^3 + ET^4$ , where  $T$  is the temperature in K

Temperature range	A (J cell <sup>-1</sup> K <sup>-1</sup> )	B (J cell <sup>-1</sup> K <sup>-2</sup> )	C (J cell <sup>-1</sup> K <sup>-3</sup> )	D (J cell <sup>-1</sup> K <sup>-4</sup> )	E (J cell <sup>-1</sup> K <sup>-5</sup> )
0–25.5 K	0	0	$-1.38753 \times 10^{-26}$	$2.27323 \times 10^{-26}$	$-3.78677 \times 10^{-28}$
25.5–120.5 K	$-1.30744 \times 10^{-22}$	$5.97279 \times 10^{-24}$	$3.79132 \times 10^{-25}$	$-4.02835 \times 10^{-27}$	$1.31661 \times 10^{-29}$
120.5–300 K	$-3.88657 \times 10^{-22}$	$2.57786 \times 10^{-23}$	$-8.0734 \times 10^{-26}$	$1.72849 \times 10^{-28}$	$-1.29846 \times 10^{-31}$

Data were converted to units of J per unit cell per Kelvin in preparation for use in the Eq. 2



approximation. Further high-pressure measurements upon mirabilite, specifically of the bulk modulus and its pressure and temperature derivatives would therefore be highly desirable to allow the determination of  $\gamma$  as a function of temperature.

The unit-cell volume thermal expansion is negative below 40 K and reaches a maximum value of  $\alpha_V \approx 110 \times 10^{-6} \text{ K}$  at 300 K. Although the volume thermal expansion gives no indication of impending dehydration near 300 K, one principal coefficient,  $\alpha_2$ , of the thermal expansion tensor exhibits a very large rate of increase approaching 300 K (as described in the following section).

### Axial expansivity

During the first warming run, the unit-cell parameter  $\beta$  (see Fig. 7) was observed to show very little variation with temperature up to 150 K ( $-5 \pm 1 \times 10^{-5} \text{ deg K}^{-1}$ ), whereafter the angle began to decrease at a much larger rate ( $-7.2 \pm 0.2 \times 10^{-4} \text{ deg K}^{-1}$ ). The decrease ceases at  $\sim 250 \text{ K}$  whereupon the angle saturates at a value of  $107.75 \pm 0.03^\circ$ . The behaviour at 150 K caused us to speculate that our initial quenching of the specimen to 80 K had locked-in the dynamic disorder (either of the deuterons or the sulfate tetrahedra) described by Levy and Lisensky (1978). As a result, we collected a second series of data upon slow cooling. Above 150 K, the behaviour of  $\beta$  during slow cooling is very similar to that on warming. However, below 150 K,  $\beta$  continued to increase, saturating in what we would consider a ‘normal’ fashion, and reaching a value at 4.2 K that is  $\sim 0.01^\circ$  larger than the quenched value. This small difference ( $\sim 10\%$  of the total variation over the range 4.2–300 K) is nonetheless clearly resolvable.

Given that we observe no evidence for disorder of the sulfate tetrahedron and its related hydrogen bonds, we conclude that the behaviour of  $\beta$  at 150 K during warming is due to ‘unlocking’ of deuteron disorder in the square rings. The change in  $\beta$  during continued warming we infer to be a proxy for the change in occupancy, the observed saturation of  $\beta$  above 250 K being due to complete disorder (50:50 occupancy of the ‘b’ and ‘c’ sites) being achieved. Since the twofold axis of rotational symmetry passes through the centre of these rings, it is logical that changes in the shape of the rings (mediated by changes in site occupancies) should influence the monoclinic angle.

The axial expansivities are largely positive over the temperature range investigated, although the *b*- and *c*-axes display a small amount of negative thermal expansion at low temperatures (below  $\sim 50 \text{ K}$ ). This behaviour is common to a number of sulfates, including  $\text{CuSO}_4 \cdot 5\text{D}_2\text{O}$ , (Schofield and Knight 2000),  $\text{MgSO}_4 \cdot 7\text{D}_2\text{O}$ , (Fortes et al.

2006b) and  $\text{MgSO}_4 \cdot 11\text{D}_2\text{O}$ , (Fortes et al. 2008b) each of which has one axis which displays negative thermal expansion. There is little discernible hysteresis between the warming and cooling data for the *a*- and *c*-axes. The small amount of hysteresis in the length of the *b*-axis may be related to the variations in  $\beta$  noted earlier. Overall, the expansivities of the *a*- and *c*-axes are of similar magnitude, whilst the *b*-axis shows a much smaller thermal expansion. In order to arrive at a better understanding of how the thermal expansion is related to structural elements in the crystal and the bonding between them, we now derive the coefficients of the thermal expansion tensor.

### Thermal expansion tensor

The thermal expansion of a monoclinic crystal is described by a symmetrical second rank tensor of the form,

$$\begin{bmatrix} \alpha_{11} & 0 & \alpha_{13} \\ 0 & \alpha_{22} & 0 \\ \alpha_{31} & 0 & \alpha_{33} \end{bmatrix} \quad (4)$$

where  $\alpha_{13} = \alpha_{31}$ . Using the Institute of Radio Engineers’ convention for the orthonormal tensor basis, where  $\mathbf{e}_3 \parallel \mathbf{c}$ ,  $\mathbf{e}_2 \parallel \mathbf{b}^*$ , and  $\mathbf{e}_1 \parallel \mathbf{e}_2 \times \mathbf{e}_3$ , then the Lagrangian thermal expansion tensor coefficients for a monoclinic crystal with *b* as the unique axis may be written in terms of the unit-cell parameters as shown below (Schlenker et al. 1975):

$$\alpha_{11}(T) = \frac{1}{a_0 \sin \beta_0} \left[ \sin \beta \frac{da}{dT} + a \cos \beta \frac{d\beta}{dT} \right] \quad (5)$$

$$\alpha_{22}(T) = \frac{1}{b_0} \frac{db}{dT} \quad (6)$$

$$\alpha_{33}(T) = \frac{1}{c_0} \frac{dc}{dT} \quad (7)$$

$$\alpha_{13}(T) = \frac{1}{a_0} \frac{da}{dT} \left[ \frac{1}{\sin 2\beta_0} - \frac{\sin \beta}{2 \cos \beta_0} \right] - \frac{a \cos \beta}{2a_0 \cos \beta_0} \frac{d\beta}{dT} - \frac{\cot \beta_0}{2c_0} \frac{dc}{dT} \quad (8)$$

In order to derive the components of the thermal expansion tensor via Eqs. (5) – (8) it is necessary to obtain suitable differentiable representatives of the cell parameters as a function of temperature. We have chosen to do this by using a modified Einstein oscillator model to fit the unit-cell data as a function of temperature rather than by using the Debye approximation described previously. Although the latter provides a more physically correct model of the behaviour of the solid than the mathematically simpler Einstein model, the functional form of the Einstein model is such that we were able to obtain a better fit to the experimental data (particularly in the regions of negative axial expansion), as required for

proper determination of the coefficients of the thermal expansion tensor. The derivation of the modified Einstein model is discussed elsewhere (see Fortes et al. 2008b); the temperature dependencies of the unit cell parameters  $a$ ,  $b$ , and  $c$ , are described by an expression of the form,

$$X(T) = X_0 + \frac{E}{(\exp(\theta_E/T) - 1)} \quad (9)$$

where  $X_0$  is the value of the fitted parameter at 0 K,  $\theta_E$  is a characteristic Einstein temperature  $= \hbar\omega_E/k_B$ , and  $E$  is the internal energy of the crystal. A sufficiently good fit (with the correct asymptotic behaviour as  $T$  tends to 0) can only be obtained when the parameter  $E$  is allowed to vary as a function of temperature,

$$E = e_0 + e_1T + e_2T^2 + e_3T^3 \quad (10)$$

such that the thermal expansion coefficient,  $\alpha = X^{-1}(\partial X/\partial T)$  is,

$$\alpha = \frac{(\exp(\theta_E/T) - 1)(3e_3T^2 + 2e_2T + e_1) + ((\theta_E/T)^2)(\exp(\theta_E/T))(e_3T^3 + e_2T^2 + e_1T + e_0)}{X(\exp(\theta_E/T) - 1)^2} \quad (11)$$

We have observed previously (Fortes et al. 2008b) that the temperature dependence of  $E$  may be understood in terms of the Grüneisen ratio being negative at low temperatures and positive at higher temperatures, finding a reasonable match to  $\gamma(T)$  in ice Ih despite the ad hoc nature of the parameterisation.

The parameters obtained from fitting Eqs. 9 (and 10) to the unit-cell volume and axial lengths are listed in Table 5 and depicted graphically in Fig. 7. For the cell parameter  $\beta$ , polynomial functions were used. The data collected on warming were fitted with a linear expression from 4 to 140 K,  $\beta(T) = a_0T + \beta_0$ , with  $a_0 = -5(1) \times 10^{-5} \text{ deg K}^{-1}$ , and  $\beta_0 = 107.8387(8)^\circ$ ; above 140 K, a polynomial of the form  $\beta(T) = a_0T^3 + \beta_0$ , with  $a_0 = -6.1(4) \times 10^{-6} \text{ deg K}^{-3}$ ,  $a_1 = 1.4(1) \times 10^{-8} \text{ deg K}^{-2}$ , and  $\beta_0 = 107.920(6)^\circ$  was used. The data collected on cooling were fitted from 4 to 300 K with a function of the form  $\beta(T) = a_0T^6 + a_1T^5 + a_2T^4 + a_3T^3 + \beta_0$ , with  $a_0 = -3.1(4) \times 10^{-15} \text{ deg K}^{-6}$ ,  $a_1 = 2.3(3) \times 10^{-12} \text{ deg K}^{-5}$ ,  $a_2 = -5.4(7) \times 10^{-10} \text{ deg K}^{-4}$ ,  $a_3 = 3.1(6) \times 10^{-8} \text{ deg K}^{-3}$ , and  $\beta_0 = 107.8474(9)^\circ$ .

Fitting the data across the full temperature range produces very large uncertainties in some of the fitted parameters, resulting in the propagation of large errors onto the thermal expansion coefficients. Better estimates of the uncertainty on these coefficients were found by linear fits to short segments of the cell parameter data; estimated  $3\sigma$  values are

$\pm 1.65 \times 10^{-6} \text{ K}^{-1}$ . The Einstein temperatures obtained here are very similar to those found by fitting to the unit cell of  $\text{MgSO}_4 \cdot 11\text{D}_2\text{O}$  (Fortes et al. 2008b),  $\theta_E$  from the volume data being  $\sim 90 \text{ K}$  for both. These very low-frequency vibrational modes, corresponding to wavenumbers of  $\sim 60 \text{ cm}^{-1}$ , which dominate the low-temperature thermal expansivity, have not been observed directly, but would be expected to be detectable in the phonon dispersion spectrum.

The modified Einstein fits to the  $a$ -,  $b$ -, and  $c$ -axes, and the polynomial fits to the angle  $\beta$ , were used to calculate the magnitudes of the thermal expansion tensor coefficients (from Eqs. 5–8) as a function of temperature. Decomposition of the tensor matrix (Eq. 4) yields the magnitude (eigenvalue) and orientation (eigenvector) of the thermal expansion tensor, i.e., the principal axes,  $\alpha_1$ ,  $\alpha_2$ , and  $\alpha_3$ . The temperature dependence of the coefficients  $\alpha_{11}$ ,  $\alpha_{22}$ ,  $\alpha_{33}$ ,  $\alpha_{13}$ , and of the principal axes  $\alpha_1$ ,  $\alpha_2$ , and  $\alpha_3$  is shown in Fig 10;  $\theta$  is the angle between  $\alpha_1$  and  $\mathbf{e}_1$ .

Projections of the representation surface of the expansion coefficients onto the three orthogonal planes,  $y$ - $z$  ( $\mathbf{e}_2$ - $\mathbf{e}_3$ ),  $x$ - $y$  ( $\mathbf{e}_1$ - $\mathbf{e}_2$ ), and  $x$ - $z$  ( $\mathbf{e}_1$ - $\mathbf{e}_3$ ), at a range of temperatures from the slow cooled data are shown in Fig. 11.

$\alpha_1$  and  $\alpha_3$  exhibit mostly positive thermal expansion at all temperatures greater than  $\sim 50 \text{ K}$ , although the values of  $\alpha_1$  are roughly an order of magnitude greater than  $\alpha_3$ . However,  $\alpha_2$  is mostly negative, and its temperature dependence is a mirror image of  $\alpha_1$ . The main difference between the warming and cooling data is a temperature offset between the two which becomes significant above 150 K; in the quenched sample,  $\alpha_1$  and  $\alpha_3$  have smaller values than the slow-cooled sample at a given temperature (above 150 K), whereas  $\alpha_2$  has a larger value. The orientation of the expansion tensor does not differ between the two data sets;  $\alpha_1$  appears to be saturating at high temperature but the large changes in  $\alpha_2$  (increase) and  $\alpha_3$  (decrease) may be signalling the impending dehydration at 305 K.

The orientation of the thermal expansion tensor undergoes a major shift (as manifested by the angle  $\theta$  between  $\mathbf{e}_1$  and  $\alpha_1$ ), swinging through  $\sim 80^\circ$  near 50 K. After this reorientation the value of  $\theta$  increases very slowly from  $+40^\circ$  to  $+50^\circ$  over the temperature range 100–300 K.

We have seen that the volumes of the various polyhedra within the mirabilite structure do not contribute greatly to

**Table 5** Parameters obtained by fitting Eqs. 9 and 10 to the unit-cell volume and cell edges of mirabilite. Note that the unit of  $X_0$  are  $\text{\AA}^3$  for the volume, and  $\text{\AA}$  for the parameters  $a$ ,  $b$ , and  $c$ : the units of  $e_0$ ,  $e_1$ ,  $e_2$ , and  $e_3$  are  $\text{\AA}^3 \text{K}^{-1}$ ,  $\text{\AA}^3 \text{K}^{-2}$ , and  $\text{\AA}^3 \text{K}^{-3}$ , respectively, for the unit cell volume, and follow the same system in  $\text{\AA}$  for the axes

	Volume (warming)	Volume (cooling)	$a$ -axis (warming)	$a$ -axis (cooling)	$b$ -axis (warming)	$b$ -axis (cooling)	$c$ -axis (warming)	$c$ -axis (cooling)
$X_0$	1436.70(2) $\text{\AA}^3$	1436.77(3) $\text{\AA}^3$	11.4421(1) $\text{\AA}$	11.4425(1) $\text{\AA}$	10.3428(2) $\text{\AA}$	10.3429(1) $\text{\AA}$	12.7533(2) $\text{\AA}$	12.7548(2) $\text{\AA}$
$\theta_E$ (K)	85(11)	78(11)	234(7)	233(6)	76(16)	92(14)	87(22)	80(17)
$e_0$	$-3.8(6)$	$-3.4(6)$	$1.3(1) \times 10^{-1}$	$1.26(9) \times 10^{-1}$	$-8(2) \times 10^{-3}$	$-1.1(2) \times 10^{-2}$	$-1.9(7) \times 10^{-2}$	$-1.6(5) \times 10^{-2}$
$e_1$	$8(1) \times 10^{-2}$	$7(1) \times 10^{-2}$	$-5.1(6) \times 10^{-4}$	$-4.6(5) \times 10^{-4}$	$1.0(3) \times 10^{-4}$	$1.2(2) \times 10^{-4}$	$3.3(1) \times 10^{-4}$	$2.8(9) \times 10^{-4}$
$e_2$	$-2.5(5) \times 10^{-4}$	$-2.0(5) \times 10^{-4}$	$1.2(1) \times 10^{-6}$	$1.1(1) \times 10^{-6}$	$-1.7(5) \times 10^{-7}$	$-1.9(4) \times 10^{-7}$	$-1.0(4) \times 10^{-6}$	$-8(3) \times 10^{-7}$
$e_3$	$3.3(7) \times 10^{-7}$	$2.7(7) \times 10^{-7}$	—	—	—	—	$1.4(7) \times 10^{-9}$	$1.1(4) \times 10^{-9}$

**Fig. 10** **a–d** (left); temperature dependence of the thermal expansion tensor coefficients,  $\alpha_{11}$ ,  $\alpha_{22}$ ,  $\alpha_{33}$  and  $\alpha_{13}$ . **e–g** (right); temperature dependence of the principal axes of the thermal expansion tensor,  $\alpha_1$ ,  $\alpha_2$ , and  $\alpha_3$ , and (panel **h**, right) the angle between  $\alpha_1$  and  $\mathbf{e}_1$ . The dotted lines are the slow cooling data, the bold lines the warming data

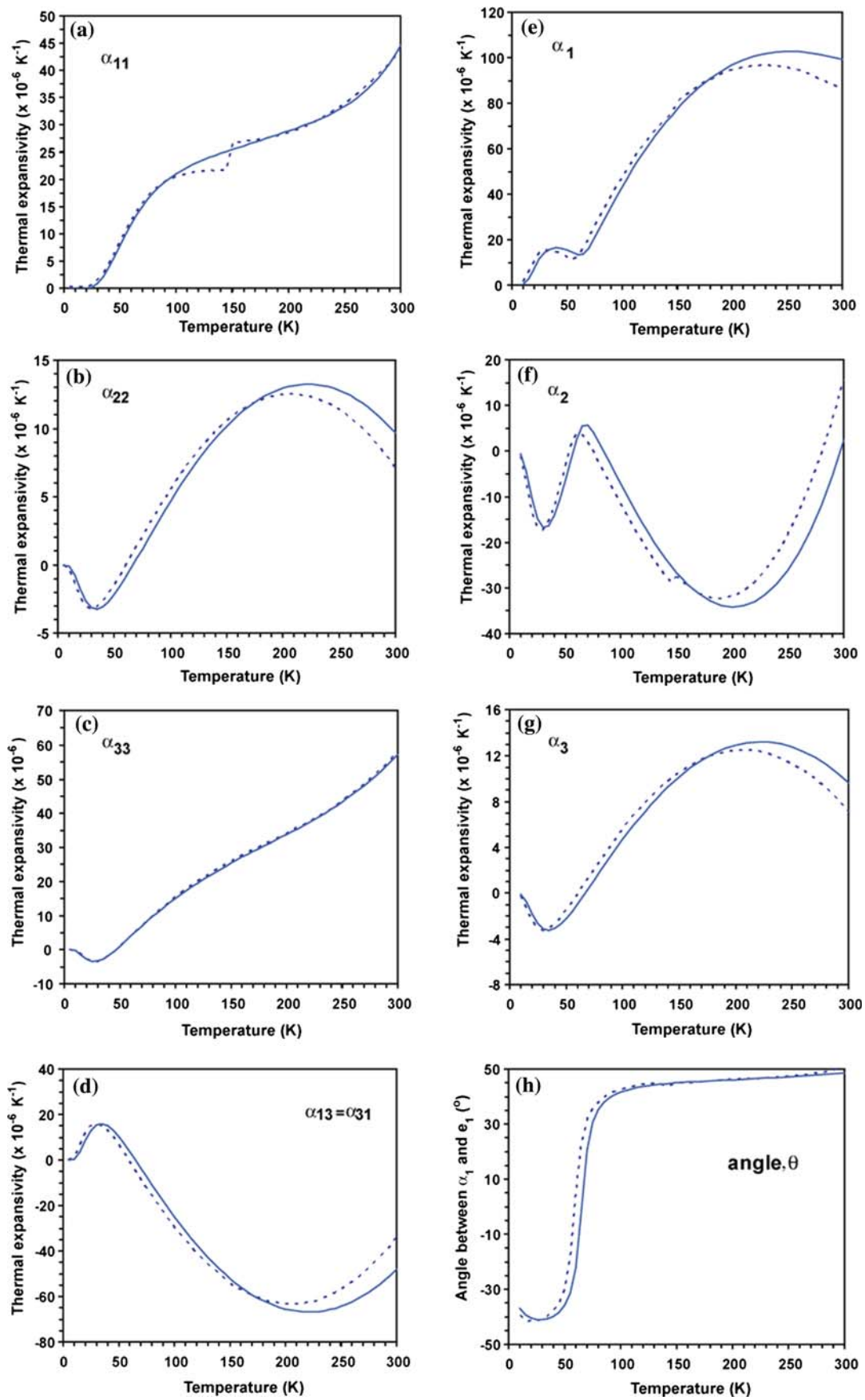
the thermal expansion; as is true of other salt hydrates that we have studied, the subtleties of the thermal expansion are controlled by the hydrogen-bond network. In gypsum, e.g., the orientation of the water molecules determines the direction of maximum thermal expansion (Schofield et al. 2004), and in meridianiite it is a weak bifurcated hydrogen bond which dominates the orientation of the expansion tensor (Fortes et al. 2008b). In mirabilite, much of the interlayer hydrogen bonding is aligned with the  $a$ -axis; it is therefore slightly surprising to find that the direction of maximum thermal expansion is inclined by more than  $30^\circ$  to this direction. It is possibly of relevance that the hydrogen bonds donated by the two interstitial water molecules O10 and O11 are more closely aligned with  $\alpha_1$  and  $\alpha_2$ , as shown in Fig. 12.

It is also possible that the reorientation of the expansion tensor is the result of shift in the relative strength of hydrogen bonds donated by these two molecules to neighbouring sulfate tetrahedra. Further detailed study of the anisotropic vibrational behaviour of the deuterons, using single-crystal neutron diffraction techniques, may yield insights into the orientation of the thermal expansion tensor.

## Summary

Time-of-flight powder neutron diffraction has been used to measure the thermal expansion of  $\text{Na}_2\text{SO}_4 \cdot 10\text{D}_2\text{O}$  from 4.2 to 300 K under ambient pressure conditions. No evidence was observed of the sulfate disorder reported previously by Levy and Lisensky (1978). The volume thermal expansion is positive above 40 K, and similar in magnitude to that of other multiply hydrated salts such as epsomite and meridianiite. A second-order Grüneisen model fitted to the data gives estimates of the elastic properties; however, future neutron powder diffraction measurements, combined with ab initio calculations, are necessary to obtain details of the elastic strain tensor at high pressure, and to determine  $\gamma(T)$  and the Anderson–Grüneisen parameter,  $\delta_T$ .

This work provides the basis for computer modelling of the structure and interpretation of high-pressure studies of this substance, as well as yielding important parameters for incorporation into structural models of icy moon interiors, and models of building stone weathering.





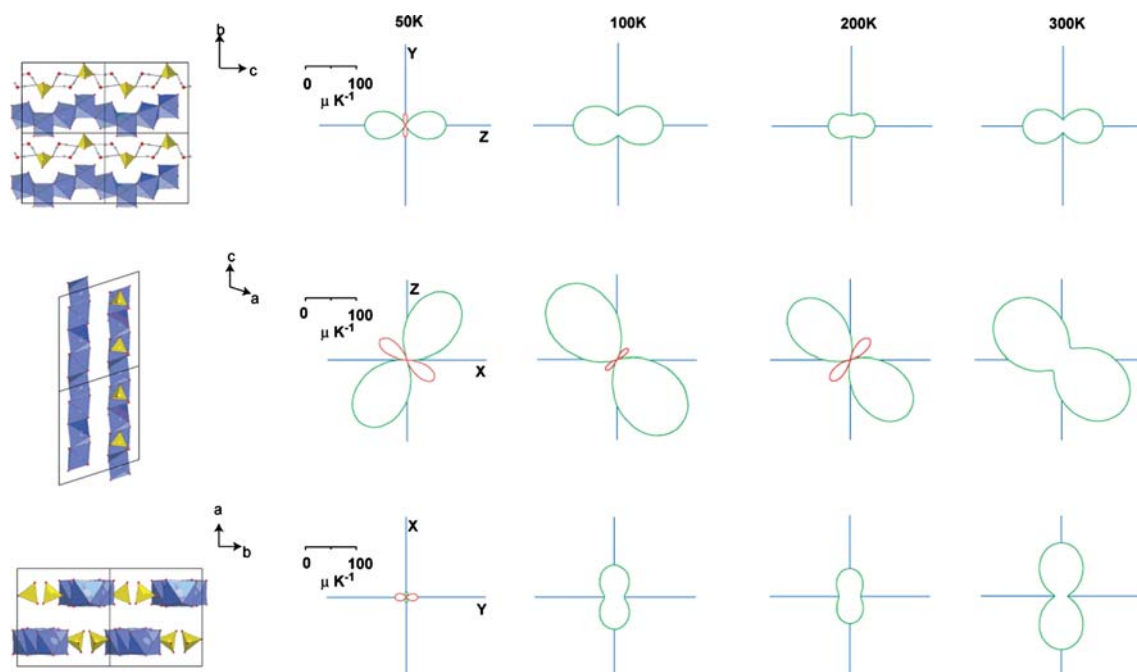


**Fig. 11** Projections of the thermal expansion coefficient representation surface on the  $y$ - $z$  ( $b$ - $c$ ) planes (*top*),  $x$ - $z$  ( $e_1$ - $c$ ) plane (*middle*), and the  $x$ - $y$  ( $e_1$ - $b$ ) plane (*bottom*) at 50, 100, 200, and 300 K. Solid green lines indicate positive values, and dotted red lines indicate

negative values. The corresponding projections of the mirabilite structure are shown on the *left*. Projections plotted using Win Tensor (Kaminsky 2004)

Science and Technology Facilities Council (STFC), UK, grant numbers PPA/P/S/2003/00247 and PP/E006515/1.

## References

- Alietti A (1959) Osservazioni sulla mirabilite di figno e sul solfato di sodio decaidrato. *Rend Acc Naz Lincei Ser 8<sup>a</sup>*, 26:689–694
- Balarew C (2002) Calculation of the free Gibbs energy of phase transitions using solubility data. 1. The system  $\text{Na}_2\text{SO}_4$ - $\text{Na}_2\text{SeO}_4$ - $\text{H}_2\text{O}$  at 15°C: stable and metastable equilibria. *Pure Appl Chem* 74(10):1793–1800. doi:[10.1351/pac200274101793](https://doi.org/10.1351/pac200274101793)
- Block EA (1913) Über die schmelzkurven einiger stoffe. *Z Phys Chem Stoich Verwandt* 82:403–438
- Braitsch O (1971) Salt deposits, their origin and composition. Springer, New York
- Brand HEA, Fortes AD, Wood IG, Alfredsson M, Vočadlo L (2006) High-pressure properties of planetary sulfate hydrates determined from interatomic potential calculations. *Lunar Planet Sci Conf 37* (abstract #1310), (<http://www.lpi.usra.edu/meetings/lpsc2006/pdf/1310.pdf>)
- Brodale GE, Giauque WF (1958) The heat of hydration of sodium sulphate. Low temperature heat capacity and entropy of sodium sulphate decahydrate. *J Phys Chem* 76(5):737–743. doi:[10.1021/j100649a024](https://doi.org/10.1021/j100649a024)
- Brooke HJ (1824) On the crystalline forms of artificial salts. *Ann Philos* 7:20–22
- Carlson RW, Calvin W, Dalton JB, Hansen GB, Hudson R, Johnson RE et al (2007) Europa's surface compositions: what we know, what we would like to know, and how we can find out. *EOS Trans Am Geophys Union* 88(54), Fall Meeting Suppl (abstract P51E-02)
- Cocco G (1962) La struttura della mirabilite. *Rend Acc Naz Lincei, Ser 8<sup>a</sup>*, 32:690–698 (ICDD entry 01-072-0495)

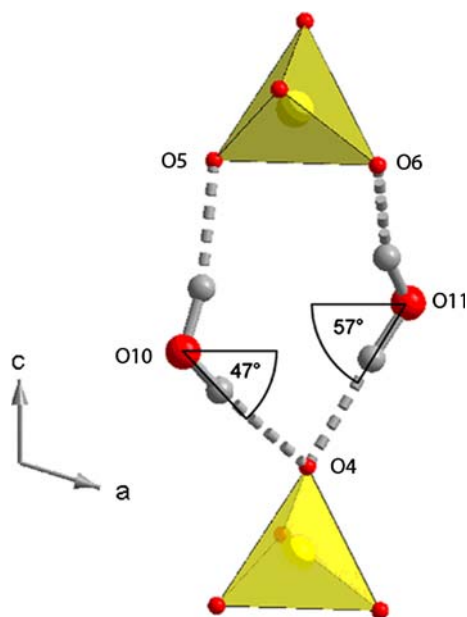


**Fig. 12** Orientations of the O10 and O11 hydrogen bonds with respect to the direction  $e_1$ , illustrating the similarity between the orientation of these bonds and the orientation of the thermal expansion tensor

**Acknowledgments** The authors wish to thank the STFC ISIS facility for beam time, and technical support staff for invaluable assistance. HEAB is funded by a postgraduate studentship from the Natural Environment Research Council; ADF is funded by the

- Cocco G, Rossetti V (1959) La cella elementare della mirabilite. *Periodico Mineral Roma* 28:231–232
- Colman SM, Kelts KR, Dinter AA (2002) Depositional history and neotectonics in Great Salt Lake, Utah, from high-resolution seismic stratigraphy. *Sediment Geol* 148(1–2):61–78. doi:10.1016/S0037-0738(01)00210-X
- Dalton JB, Prieto-Ballesteros O, Kargel JS, Jamieson CS, Jolivet J, Quinn R (2005) Spectral comparison of heavily hydrated salts with disrupted terrains on Europa. *Icarus* 177(2):472–490. doi:10.1016/j.icarus.2005.02.023
- De Coppet L-C (1907) Recherches sur la surfusion et la sursaturation. *Ann Chim Phys* 8<sup>me</sup> Sér 10:457–527
- Dougherty AJ, Hogenboom DL, Kargel JS, Zheng YF (2006) Volumetric and optical studies of high pressure phases of  $\text{Na}_2\text{SO}_4 \cdot 10\text{H}_2\text{O}$  with applications to Europa. *Lunar Planet Sci Conf 37* (abstract #1732). (<http://www.lpi.usra.edu/meetings/lpsc2006/pdf/1732.pdf>)
- Finger LW, Kroecker M, Toby BH (2007) DRAWxtl, an open-source computer program to produce crystal structure drawings. *J Appl Cryst* 40:188–192. doi:10.1107/S0021889806051557
- Finney JL (1995) The complimentary use of X-ray and neutron diffraction in the study of crystals. *Acta Crystallogr Sect B Struct Sci B* 51:447–467. doi:10.1107/S0108768195002734
- Fortes AD, Wood IG, Grigoriev D, Alfredsson M, Kipfstuhl S, Knight KS et al (2004) No evidence of large-scale proton ordering in Antarctic ice from powder neutron diffraction. *J Chem Phys* 120(24):11376–11379. doi:10.1063/1.1765099
- Fortes AD, Wood IG, Vočadlo L, Brand HEA, Grindrod PM, Joy KH, et al. (2006a) The phase behaviour of epsomite ( $\text{MgSO}_4 \cdot 7\text{H}_2\text{O}$ ) to 50 kbar: planetary implications. *Lunar Planet. Sci. Conf. 37*, abstract #1029 (<http://www.lpi.usra.edu/meetings/lpsc2006/pdf/1029.pdf>)
- Fortes AD, Wood IG, Alfredsson M, Vočadlo L, Knight KS (2006b) The thermoelastic properties of  $\text{MgSO}_4 \cdot 7\text{D}_2\text{O}$  (epsomite) from powder neutron diffraction and ab initio simulation. *Eur J Min* 18(4):449–462. doi:10.1127/0935-1221/2006/0018-0449
- Fortes AD, Wood IG, Knight KS (2006c) Neutron powder diffraction studies of sulfuric acid hydrates. I: The structure of sulfuric acid hemitriskaidkahydrate,  $\text{D}_2\text{SO}_4 \cdot 6\frac{1}{2}\text{D}_2\text{O}$ . *J Chem Phys* 125(14):144510. doi:10.1063/1.2356860
- Fortes AD, Grindrod PM, Trickett SK, Vočadlo L (2007a) Ammonium sulfate on Titan: possible origin and role in cryovolcanism. *Icarus* 188(1):139–153. doi:10.1016/j.icarus.2006.11.002
- Fortes AD, Wood IG, Vočadlo L, Brand HEA, Knight KS (2007b) Crystal structures and thermal expansion of  $\alpha$ - $\text{MgSO}_4$  and  $\beta$ - $\text{MgSO}_4$  from 4.2–300 K by neutron powder diffraction. *J Appl Cryst* 40(4):761–770. doi:10.1107/S0021889807029937
- Fortes AD, Wood IG, Vočadlo L, Knight KS (2008a) Neutron diffraction studies of sulfuric acid hydrates. II: The structure, thermal expansion, incompressibility and polymorphism of sulfuric acid tetrahydrate ( $\text{D}_2\text{SO}_4 \cdot 4\text{D}_2\text{O}$ ). *J Chem Phys* 128(6) article 054506 doi:10.1063/1.2827474
- Fortes AD, Wood IG, Knight KS (2008b) The crystal structure and thermal expansion tensor of  $\text{MgSO}_4 \cdot 11\text{D}_2\text{O}$  (meridianiite) determined by neutron powder diffraction. *Phys Chem Miner* 35(4):207–221. doi:10.1007/s00269-008-0214-x
- Gans W (1978) Thermodynamic stability of sodium sulfate heptahydrate. *Z Phys Chem* 111(1):39–46
- Garrett DE (2001) Sodium sulfate: handbook of deposits, processing, properties, and use. Academic Press, London
- Geller A (1924) Über das verhalten verschiedener minerale der salzlager bei hohen drucken und wechselnden temperaturen. *Z Krist* 60:415–472
- Genkinger S, Putnis A (2007) Crystallisation of sodium sulfate: supersaturation and metastable phases. *Environ Geol* 52:329–337. doi:10.1007/s00254-006-0565-x
- Glauber JH (1658) *Tractatus de natura salium*. Amsterdam
- Goudie AS, Viles H (1997) *Salt weathering hazards*. Wiley, Chichester
- von Groth P (1908) *Chemische Kristallographie, Teil 2: Die anorganischen oxo- und sulfosalze*. Leipzig. pp 371–372
- Hanawalt JD, Rinn HW, Frevel LK (1938) Chemical analysis by X-ray diffraction. *Ind Eng Chem Anal Edn* 10(9):457–512 (doi:10.1021/ac50125a001) (ICDD entry 00-001-0207)
- Hardie LA (1991) On the significance of evaporites. *Annu Rev Earth Planet Sci* 19:131–168. doi:10.1146/annurev.ea.19.050191.001023
- Hartley H, Jones BM, Hutchinson GA (1908) The spontaneous crystallisation of sodium sulphate solutions. *J Chem Soc* 93:825–833. doi:10.1039/CT9089300825
- Hill AE, Wills JH (1938) Ternary systems. XXIV, calcium sulphate, sodium sulphate and water. *J Am Chem Soc* 60(7):1647–1655. doi:10.1021/ja01274a037
- Hogenboom DL, Kargel JS, Pahalawatta PV (1999) Densities and phase relationships at high pressures of the sodium sulfate-water system. *Lunar Planet Sci Conf 30* (abstract #1793)
- Ibberson RM, David WIF, Knight KS (1992) The high resolution neutron powder diffractometer (HRPD) at ISIS—a user guide. RAL-92-031. Rutherford Appleton Laboratory, Oxfordshire ([http://www.isis.rl.ac.uk/crystallography/documentation/HRPD\\_guide](http://www.isis.rl.ac.uk/crystallography/documentation/HRPD_guide))
- Kaminsky W (2004) WinTensor 1.1. (<http://www.wintensor.com>)
- Kargel JS (1991) Brine volcanism and the interior structure of asteroids and icy satellites. *Icarus* 94(2):368–390. doi:10.1016/0019-1035(91)90235-L
- Keys JR, Williams K (1981) Origin of crystalline, cold desert salts in the McMurdo region, Antarctica. *Geochim Cosmochim Acta* 45(12):2299–2309. doi:10.1016/0016-7037(81)90084-3
- Kryukov PA, Manikhin VI (1960) Characteristics of the melting of glauber salt at high pressure. *Russ Chem Bull* 9(12):2077–2078. doi:10.1007/BF00912067
- Larsen AC, Von Dreele RB (2000) General structure analysis system (GSAS). Los Alamos National Laboratory Report LAUR 86-748, Los Alamos, New Mexico (<http://www.ncnr.nist.gov/xtal/software/gsas.html>)
- Levy HA, Lisensky GC (1978) Crystal structures of sodium sulfate decahydrate (Glauber's salt) and sodium tetraborate decahydrate (borax). Redetermination by neutron diffraction. *Acta Cryst Sect B Struct Sci* 34:3502–3510. doi:10.1107/S0567740878011504 (ICDD entry 01-075-1077)
- Löwel H (1850) Observations sur la sursaturation des dissolution salines. Premier mémoire. *Ann Chim Phys* 3<sup>me</sup> Sé 29:62–127
- Löwel H (1851) Observations sur la sursaturation des dissolution salines. Deuxième mémoire. *Ann Chim Phys* 3<sup>me</sup> Sér 33:334–390
- Löwel H (1853) Observations sur la sursaturation des dissolution salines. Troisième mémoire. *Ann Chim Phys* 3<sup>me</sup> Sér 37:155–179
- Löwel H (1857) Observations sur la sursaturation des dissolution salines. Sixième mémoire. *Ann Chim Phys* 3<sup>me</sup> Sér 49:32–57
- Marliacy P, Solimando R, Bouroukba M, Schuffenecker L (2000) Thermodynamics of crystallization of sodium sulfate decahydrate in  $\text{H}_2\text{O}$ – $\text{NaCl}$ – $\text{Na}_2\text{SO}_4$ : application to  $\text{Na}_2\text{SO}_4 \cdot 10\text{H}_2\text{O}$ -based latent heat storage materials. *Thermochim Acta* 344(1–2):85–94. doi:10.1016/S0040-6031(99)00331-7
- Negi AS, Anand SC (1985) *A textbook of physical chemistry*. New Age Publishers, Watertown
- Orlando TM, McCord TB, Grieses GA (2005) The chemical nature of Europa's surface material and the relation to a subsurface ocean. *Icarus* 177(2):528–533. doi:10.1016/j.icarus.2005.05.009
- Palache C, Berman H, Frondel C (1951) *Dana's system of mineralogy*. 7th edn, vol II, pp 439–442

- Pitzer KS, Coulter LV (1938) The heat capacities, entropies, and heats of solution of anhydrous sodium sulfate and of sodium sulfate decahydrate. The application of the third law of thermodynamics to hydrated crystals. *J Am Chem Soc* 60(6):1310–1313. doi:[10.1021/ja01273a010](https://doi.org/10.1021/ja01273a010)
- Rasmussen SE, Jorgensen JE, Lundtoft B (1996) Structures and phase transitions of  $\text{Na}_2\text{SO}_4$ . *J Appl Cryst* 29(1):42–47. doi:[10.1107/S0021889895008818](https://doi.org/10.1107/S0021889895008818)
- Rijniers LA, Huinink HP, Pel L, Kopinga K (2005) Experimental evidence of crystallisation pressure inside porous media. *Phys Rev Lett* 94:075503. doi:[10.1103/PhysRevLett.94.075503](https://doi.org/10.1103/PhysRevLett.94.075503)
- Robinson K, Gibbs GV, Ribbe PH (1971) Quadratic elongation: a quantitative measure of distortion in coordination polyhedra. *Science* 172:567–570. doi:[10.1126/science.172.3983.567](https://doi.org/10.1126/science.172.3983.567)
- Rosicky V (1908) Beiträge zur morphologie der glaubersalzsreihe. *Z Krist* 45:473–489
- Röttger K, Endriss A, Ihringer J (1994) Lattice constants and thermal expansion of  $\text{H}_2\text{O}$  and  $\text{D}_2\text{O}$  ice Ih between 10 and 265 K. *Acta Crystallogr B* 50:644–648. doi:[10.1107/S0108768194004933](https://doi.org/10.1107/S0108768194004933)
- Rubens HW, Templeton DH, Rosenstein RD, Olovsson I (1961) Crystal structure and entropy of sodium sulfate decahydrate. *J Am Chem Soc* 83(4):820–824. doi:[10.1021/ja01465a019](https://doi.org/10.1021/ja01465a019) (ICDD entry 01-074-0937)
- Schofield PF, Knight KS (2000) Neutron powder diffraction studies of the thermal behaviour of deuterated chalcantite. *Physica B* 276–278:897–898. doi:[10.1016/S0921-4526\(99\)01282-X](https://doi.org/10.1016/S0921-4526(99)01282-X)
- Schlenker JL, Gibbs GV, Boison MB (1975) Thermal expansion coefficients for monoclinic crystals: a phenomenological approach. *Am Min* 60:823–833
- Schofield PF, Knight KS, van der Houwen JAM, Valsami-Jones E (2004) The role of hydrogen bonding in the thermal expansion and dehydration of brushite, di-calcium phosphate dihydrate. *Phys Chem Miner* 31(9):606–624. doi:[10.1007/s00269-004-0419-6](https://doi.org/10.1007/s00269-004-0419-6)
- Tammann G (1929) Über die schmelzkurven einiger salzhhydrate. *Z Anorg Allg Chem* 179(1):186–192. doi:[10.1002/zaac.19291790114](https://doi.org/10.1002/zaac.19291790114)
- Tanaka Y, Hada S, Makita T, Moritoki M (1992) Effect of pressure on the solid–liquid phase equilibria in (water + sodium sulphate) system. *Fluid Phase Equil* 76:163–173. doi:[10.1016/0378-3812\(92\)85085-M](https://doi.org/10.1016/0378-3812(92)85085-M)
- Toby BH (2001) EXPGUI, a graphical user interface for GSAS. *J Appl Cryst* 34:210–213. doi:[10.1107/S0021889801002242](https://doi.org/10.1107/S0021889801002242)
- Tomlinson C (1868) On supersaturated saline solutions. *Philos Trans R Soc Lond* 158:659–673. doi:[10.1098/rstl.1868.0028](https://doi.org/10.1098/rstl.1868.0028)
- Tomlinson C (1871) On the behaviour of supersaturated saline solutions when exposed to the open air. *Proc R Soc Lond* 20:41–45. doi:[10.1098/rspl.1871.0013](https://doi.org/10.1098/rspl.1871.0013)
- Tsui N, Flatt RJ, Scherer GW (2003) Crystallization damage by sodium sulphate. *J Cult Herit* 4:109–115. doi:[10.1016/S1296-2074\(03\)00022-0](https://doi.org/10.1016/S1296-2074(03)00022-0)
- Viollette C (1866) Mémoire sur la sursaturation. *Ann Sci Ecole Normale Super* 30:202–252
- Vočadlo L, Knight KS, Price GD, Wood IG (2002) Thermal expansion and crystal structure of FeSi between 4 K and 1173 K determined by time of flight neutron powder diffraction. *Phys Chem Miner* 29(2):132–139. doi:[10.1007/s002690100202](https://doi.org/10.1007/s002690100202)
- Wallace DG (1998) Thermodynamics of crystals. Dover, New York
- Washburn ER, Clem WJ (1938) The transition temperature of sodium sulfate heptahydrate. *J Am Chem Soc* 60:754–757. doi:[10.1012/ja01271a007](https://doi.org/10.1012/ja01271a007)
- Wood IG, Knight KS, Price GD, Stuart JA (2002) Thermal expansion and atomic displacement parameters of cubic  $\text{KMgF}_3$  perovskite determined by high resolution neutron powder diffraction. *J Appl Cryst* 35:291–295. doi:[10.1107/S0021889802002273](https://doi.org/10.1107/S0021889802002273)
- Wuite JP (1914) The sodium sulphate–water system. *Z Phys Chem Stoich Verwandt* 86:349–382